Effects of pulse-like ground motions on tunnels in saturated poroelastic soil for obliquely incident seismic waves

Jun Zhu[1], Xiaojun Li[1,*], Jianwen Liang[2], Stavroula Kontoe[3,4], Qiumei He[5], Su Chen[1]

1. *Beijing Key Laboratory of Earthquake Engineering and Structural Retrofit, Beijing University of Technology, Beijing 100124, China*
2. *Department of Civil Engineering, Tianjin University, Tianjin 300354, China*
3. *Department of Civil Engineering, University of Patras, Greece*
4. *Department of Civil & Environmental Engineering, Imperial College London, UK*
5. *Institute of Geophysics, China Earthquake Administration, Beijing, 100081, China*

Abstract: It has been widely recognised that near-fault ground motions can be distinctly different from far-fault ground motions, in terms of their amplitudes and spectral characteristics, and there are a number of studies investigating the effects of near-fault ground motions on the structural response. However, only a few studies focus on underground tunnels, and most of them consider vertically incident seismic waves, neglecting the wave passage effect which is critical for long tunnels. This paper investigates the consequences of near-fault pulse-like ground motions on the seismic tunnel response, with an example of a tunnel embedded in saturated poroelastic soil. The input motions are represented by obliquely incident P1 waves, and the wave passage effect along the longitudinal direction is considered by a 2.5D modelling technique. The seismic tunnel response for near-fault pulse-like and far-fault ground motions is compared. Additionally, artificial ground motions, which have consistent acceleration response spectra with the near-fault pulse-like ground motions, but without velocity pulses, are generated to gain further insight into the contribution of velocity pulses. It is shown that the near-fault pulse-like ground motions can noticeably increase the tunnel internal forces, due to large seismic energy associated with the velocity pulses. For pulse-like ground motions with similar acceleration response spectra, the fling-step velocity pulse can be more detrimental to the tunnel than the forward-directivity velocity pulse. Moreover, the amplification effect of the near-fault pulse-like ground motions on the tunnel internal forces tends to be more prominent for large vertical angles of incidence, highlighting the significance of considering the oblique incidence case for seismic design.

Keywords: Underground tunnels; Near-fault pulse-like ground motions; Forward-directivity velocity pulse; Fling-step velocity pulse; Wave passage effect; Saturated poroelastic soil

*Corresponding author
E-mail: beerli@vip.sina.com (Xiaojun Li)

1. Introduction

Strong far-fault ground motions are usually considered for the seismic design of engineering structures. However, severe damage to engineering structures in near-fault regions has been observed during recent earthquakes, such as the 1994 Northridge, 1995 Kobe, 1999 Duzce and Chi-Chi, and 2008 Wenchuan earthquakes. The near-fault ground motions can be very different from the far-fault ground motions; they may have the hanging-wall effect, directivity effect, significant vertical ground motion, and large velocity pulses [1-9]. Among them, the large velocity pulses of near-fault ground motions aroused considerable attention, which can be very destructive to structures as they usually carry significant seismic energy [10-14]. The velocity pulses can be divided into two categories according to the fault rupture mechanism: (i) the forward-directivity velocity pulse characterised by a prominent double-sided velocity pulse, which is generated when the fault rupture propagates forward toward the observation site with a velocity close to the shear-wave velocity of the site; (ii) the fling-step velocity pulse characterised by a significant one-sided velocity pulse, which is associated with the residual ground displacement resulting from the relative movement of the hanging wall and foot wall.

There have been a number of studies on the structural response for near-fault pulse-like ground motions, focusing mostly on aboveground buildings or bridges. Relevant studies can be generally grouped into two categories according to their research topics: (1) comparative studies on the structural response between near-fault pulse-like and far-fault ground motions (e.g., [15,16]), evaluating the overall influence of the velocity pulses; (2) parametric investigation on the effects of pulse parameters on the structural response (e.g., [17-22]), with particular emphasis on the peak pulse velocity and pulse period. With regard to underground structures, only a few studies involve near-fault pulse-like ground motions. Case studies of damaged tunnels in near-fault regions were conducted by post-earthquake field observations or numerical simulations to reveal their seismic performance for near-fault ground motions [23-26]. Using the continuous wavelet analysis to decompose a representative near-fault ground motion record into a pulse-like component and a residual non-pulse component, Qiu et al. [27]

numerically investigated the influence of the velocity pulses on the seismic response of an underground large-scale frame structure. The effects of the near-fault pulse-like, near-fault non-pulse, and far-field ground motions on the seismic stability of an underground rock cavern with geological discontinuities are compared by Cui et al. [28] using a discrete element method. Also by selecting typical near-fault pulse-like, near-fault non-pulse, and far-field ground motions, Chen and Wei [29] investigated the correlation between ground motion parameters and lining damage indices for mountain tunnels. By the incremental dynamic analysis, Sun et al. [30] compared the fragility curves of arched hydraulic tunnels for near-fault pulse-like and far-fault ground motions. They found that the ratio of the peak ground velocity (PGV) to the peak ground acceleration (PGA) is a critical factor that affects the seismic performance of the hydraulic tunnel, and the forward-directivity pulse-like ground motions with high PGV/PGA ratios tend to cause severer damage to the hydraulic tunnel compared to those with low PGV/PGA ratios. Apart from numerical studies, the effects of the near-fault pulse-like ground motions are also investigated by laboratory experiments. Chen et al. [31] performed a series of shaking table tests of a multi-story subway station, and the experimental measurements highlight the influence of rich low-frequency content and high energy of the near-fault pulse-like ground motions. Yang et al. [32] investigated the seismic response of a segmental tunnel in the sand under near-fault ground motions by a 1 g shaking table test, concluding that the near-fault ground motions result in significant shear strains in the soil and thus further induce large seismic tunnel response.

Many tunnels are constructed in near-fault regions, as they are often kilometers long and have limited flexibility in the selection of their construction location. To this end, studies on the influence of near-fault ground motions are significant to seismic design. In spite of the above-mentioned developments in this field, the behaviour of underground tunnels subjected to near-fault pulse-like ground motions has not been thoroughly understood and needs further investigation. This study aims to investigate the seismic response characteristics of tunnels subjected to obliquely incident near-fault pulse-like waves. The angle of incidence is a critical factor that determines the seismic tunnel response

[33-38], as the associated wave passage effect may cause significant longitudinal deformation in the tunnel lining. Such effects of near-fault pulse-like ground motions have seldomly been investigated previously. In addition, the effects of the velocity pulses are usually investigated by comparing the structural response for near-fault pulse-like ground motions with that for far-fault ground motions. However, natural earthquake records have not only different velocity peaks but also distinct spectral characteristics. This study goes further than previously, investigating the contribution of the velocity pulses by excluding the influence of the spectral characteristics, aiming to identify and distinguish the effects of the two types of velocity pulses (i.e., the forward-directivity and fling-step velocity pulses). Our approach towards this goal is a comparative study on the seismic tunnel response between the near-fault pulse-like ground motions and artificial ground motions, which have consistent acceleration response spectra with the near-fault pulse-like ground motions, but without velocity pulses.

The considered soil-tunnel system for obliquely incident seismic waves is illustrated in Fig. 1. The direction of the incident seismic waves are represented by two angles: the horizontal angle of incidence θ_h (see Fig. 1(b)), which is the angle between the y-axis and the y'-axis (i.e., the projection of the propagation direction of the incident waves in the x-o-y plane), and the vertical angle of incidence θ_v (see Fig. 1(c)), which is the angle between the z-axis and the projection of the propagation direction of the incident waves in the y'-o-z plane. Compared with a vertical incidence case, which is usually considered in the existing studies, the oblique incidence case can contribute to a more comprehensive understanding of the seismic tunnel response, as it takes into account the wave passage effect, which plays an essential role in the seismic design of long tunnels. Moreover, the oblique incidence case is more realistic for near-fault regions, given limited distances between the hypocenter and near-fault engineering sites.

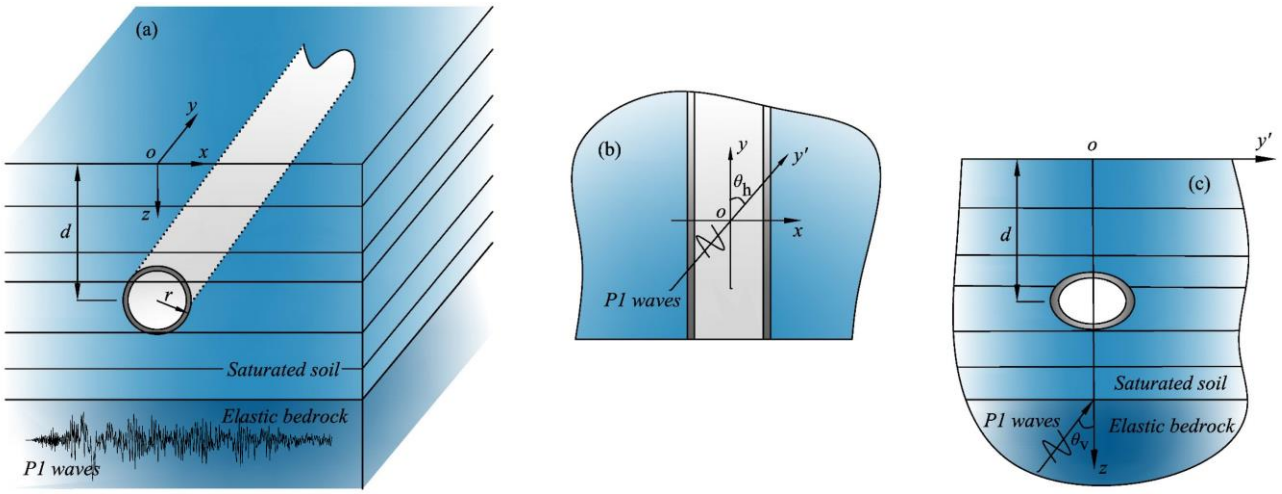


Fig. 1. (a) The model of a circular tunnel in a horizontally layered half-space subjected to obliquely incident seismic waves, (b) the *x*-*o*-*y* plane view illustrating the horizontal angle of incidence θ_h, and (c) the *y*'-*o*-*z* plane view illustrating the vertical angle of incidence θ_v.

Tunnels may be deeply buried in the soil and under the groundwater level, and it would be more rigorous to model the soil below the groundwater level as a two-phase medium (i.e., saturated poroelastic soil). The combined effect of the velocity pulses and obliquely incident seismic waves on tunnels embedded in saturated soil has not been examined previously, while it may be critical for coastal earthquake-prone regions. The input motion is represented by P1 waves (i.e., fast compressional waves), as the coupling effect of the solid skeleton and pore water can be significant under compressive loading, and an undrained single-phase simulation cannot accurately capture this two-phase coupling effect [39]. It is worth mentioning that although the incoming waves is considered as P1 waves, there also exist P2 waves (i.e., the slow compressional waves) due to the relative pore water to solid skeleton movement, and the situation is more complex due to the mode conversion at the free surface and interfaces between the soil layers, resulting in simultaneous existence of P1, P2, and SV waves in the multi-layered half-space.

In the next section, the input ground motion for this study is presented and introduced, including typical near-fault pulse-like and far-fault ground motions, as well as artificial non-pulse ground motions. The dynamic soil-tunnel interaction for obliquely incident seismic waves is simulated by a 2.5D finite element and boundary element (FE-BE) coupling method, which is described and verified

in Section 3, followed by the results and analysis in Section 4, where the effects of near-fault pulse-like ground motion on the seismic tunnel response are investigated in detail.

2. Input ground motions

This section introduces the input ground motions for the numerical study. Typical near-fault pulse-like and far-fault ground motions are first selected for a comparative study. Then, artificial ground motions, which have consistent acceleration response spectra with the near-fault pulse-like ground motions, but without velocity pulses, are generated to further evaluate the contribution of the velocity pulses.

2.1 Selected near-fault pulse-like and far-fault ground motions

Table 1 presents the details of the selected ground motion records from the PEER Ground Motion Database (https://ngawest2.berkeley.edu/), including three forward-directivity pulse-like ground motions (referred to as A1, A2, and A3 records), three fling-step pulse-like ground motions (referred to as B1, B2, and B3 records), and three far-fault ground motions (referred to as C1, C2, and C3 records). The near-fault pulse-like ground motions were selected by the following criteria: (i) the Joyner-Boor distance, R_{jb}, is less than 15 km; (ii) the duration of the velocity pulse is longer than 0.5 s; (iii) the largest peak velocity is at least twice as large as the secondary peak velocity; otherwise, the secondary peak velocity should be at least twice as large as the other peak velocities. The selection of the far-fault ground motions follows the recommendations of Kalkan and Kunnath [15]. The three far-fault ground motions have Joyner-Boor distances in the range of 19 to 40 km and significantly smaller PGV values than the near-fault pulse-like ground motions. Moreover, among the selected ground motions, the near-fault pulse-like ones have PGV/PGA ratios larger than 0.2, with the exception of the fling-step pulse-like ground motion B3, which has a PGV/PGA ratio equal to 0.14, while the far-fault ground motions have far smaller PGV/PGA ratios of around 0.1.

Table 1
Details of the selected ground motions.

No.	Earthquake	Station	Compo.	M_W	R_{jb} (km)	PGA (g)	PGV (cm/s)
Forward-directivity pulse-like ground motions							
A1	Northridge (1994)	Newhall-W. Pico Canyon Rd.	046	6.7	2.11	0.46	92.77
A2	Imperial Valley (1979)	E07	230	6.5	0.56	0.46	109.27
A3	Imperial Valley (1979)	E04	230	6.5	4.9	0.36	76.53
Fling-step pulse-like ground motions							
B1	Chi-Chi (1999)	TCU75	EW	7.6	0.89	0.35	116.21
B2	Chi-Chi (1999)	TCU76	EW	7.6	2.74	0.33	69.10
B3	Chi-Chi (1999)	TCU129	EW	7.6	1.83	0.51	68.20
Far-fault ground motions							
C1	Kern country (1952)	Taft Lincoln School	111	7.4	38.4	0.18	19.40
C2	San Fernando (1971)	Castaic-Old Ridge Route	291	6.6	19.3	0.28	30.18
C3	Northridge (1994)	Saturn Street School	S70E	6.7	26.9	0.43	42.04

To exclude the influence of the earthquake intensity, the peak accelerations of all the selected ground motions are scaled to 0.2 g. Figs. 2~4 show the scaled acceleration and velocity time histories of the selected ground motions. Distinctive double-sided and one-sided velocity pulses are found for the forward-directivity and fling-step pulse-like ground motions, respectively, and the peak velocities of the far-fault ground motions are considerably smaller than those of the near-fault ground motions.

Fig. 5 shows the acceleration response spectra of the forward-directivity pulse-like, fling-step pulse-like, and far-fault ground motions, as well as the mean spectra for each type of the selected ground motions. For periods beyond 1 s, both types of the pulse-like ground motions have noticeably larger mean spectral accelerations than the far-fault ground motions, which is a typical characteristic of pulse-like ground motions [16]. In addition, the acceleration response spectra of the two types of pulse-like ground motions present significant differences. The mean spectrum of the three forward-directivity pulse-like ground motions has a distinct platform portion in the period range of 1 s and has higher ordinates in the longer period range than the mean spectrum of the three fling-step pulse-like ground motions.

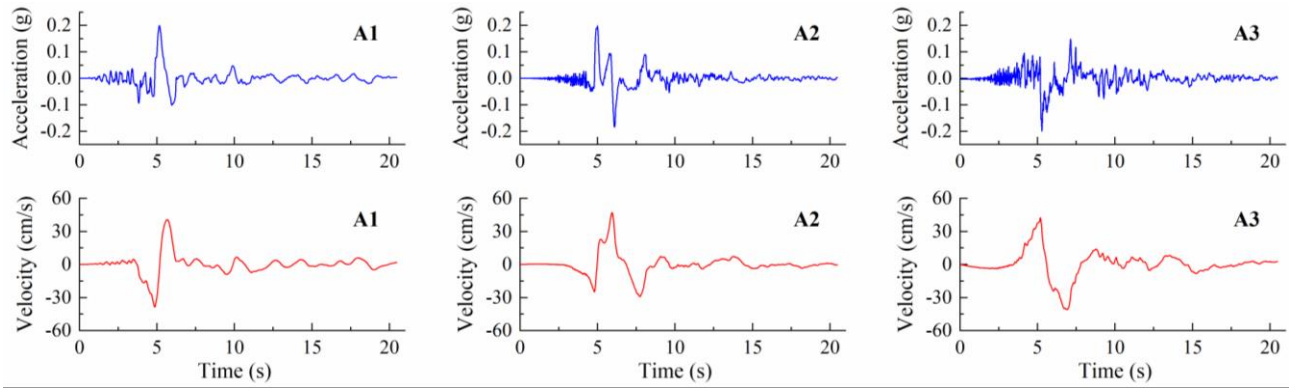


Fig. 2. Scaled acceleration and velocity time histories of the forward-directivity pulse-like ground motions.

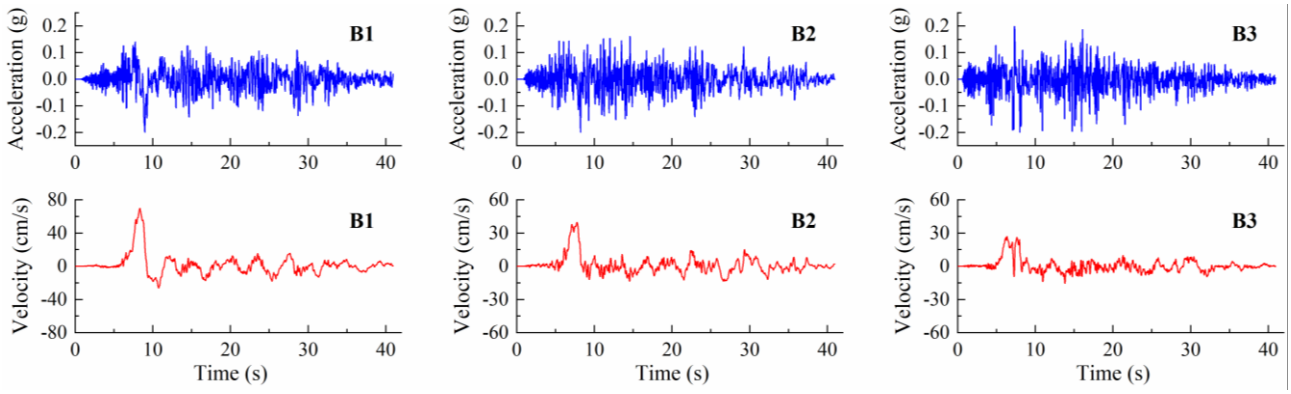


Fig. 3. Scaled acceleration and velocity time histories of the fling-step pulse-like ground motions.

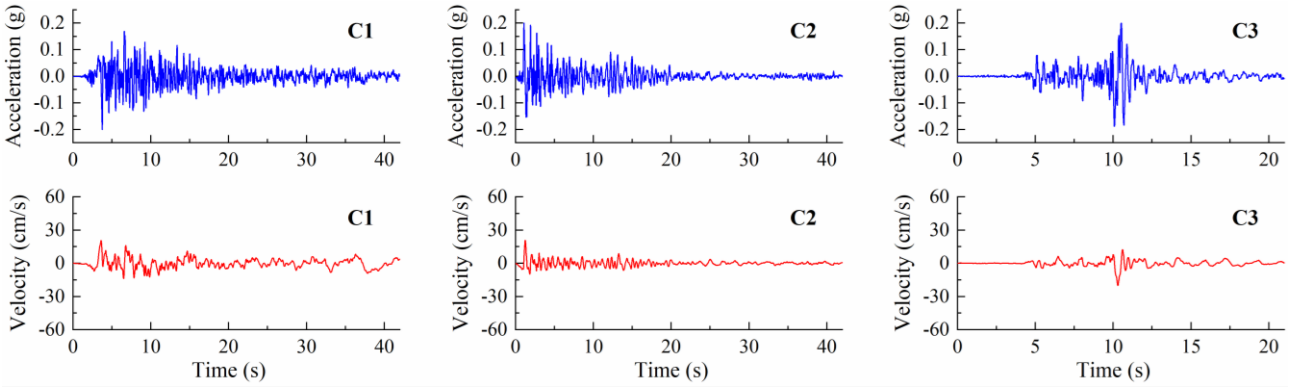


Fig. 4. Scaled acceleration and velocity time histories of the far-fault ground motions.

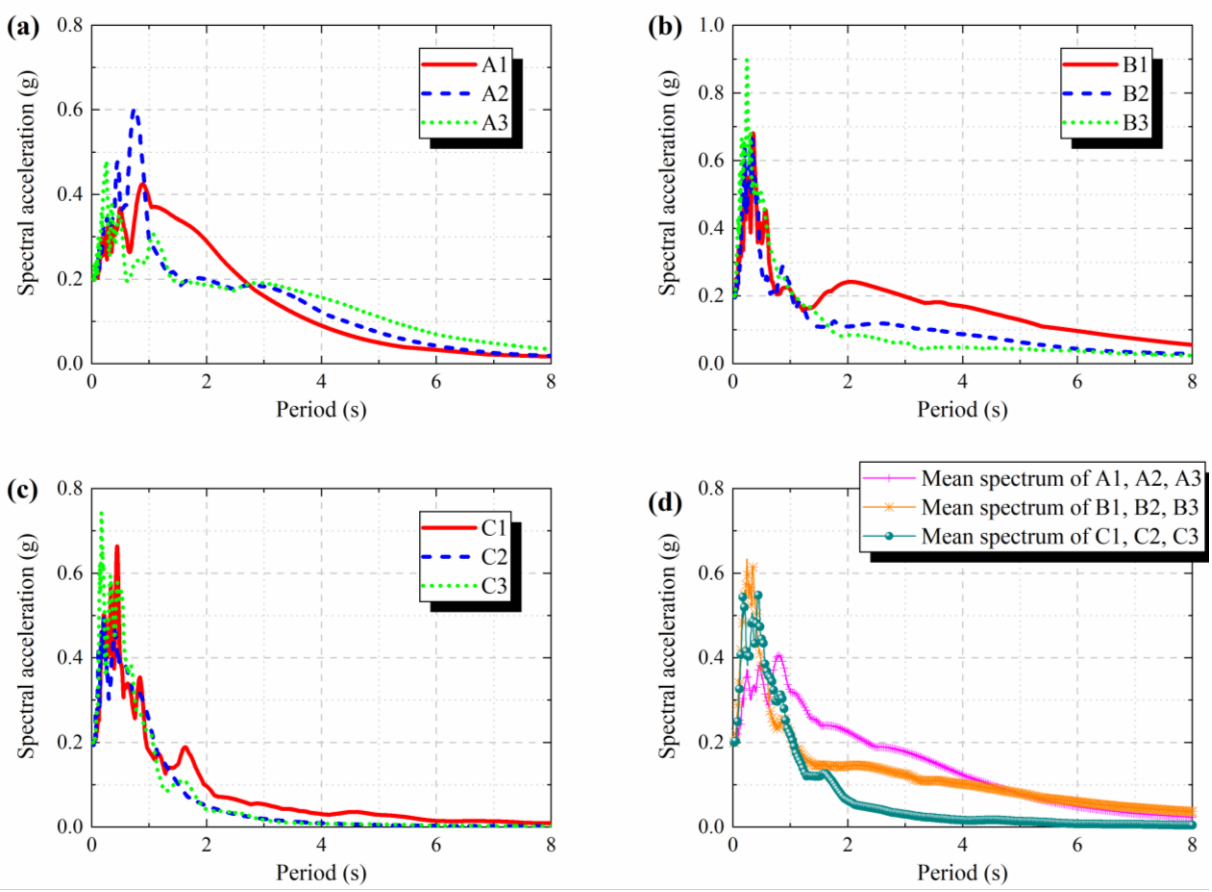


Fig. 5. Spectral accelerations (5% damping) for (a) the forward-directivity pulse-like ground motions, (b) fling-step pulse-like ground motions, and (c) far-fault ground motions, and (d) mean spectral accelerations for the three types of ground motions.

2.2 Artificial non-pulse ground motions

Artificial non-pulse ground motions are used to quantitatively identify the effects of the velocity pulses of the near-fault ground motions. Three acceleration time histories are generated for each of the six near-fault pulse-like ground motions as follows. First, an initial acceleration time history is generated according to the target peak ground acceleration, acceleration response spectrum, and intensity envelope, using trigonometric series with an iterative procedure [40]. Then, the initial acceleration time history is further adjusted such that its peak ground velocity approaches the targeted one, which is achieved by modifying the Fourier amplitudes of the initial acceleration time history [41]. As shown in Fig. 6, the acceleration time histories aj1, aj2, and aj3 (j = 1, 2, and 3) are generated according to the acceleration response spectra of the forward-directivity pulse-like ground motions Aj. The corresponding velocity time histories of the artificial non-pulse ground motions are also plotted

in Fig. 6, and the peak velocities of a*j*1, a*j*2, and a*j*3, respectively, are about 90%, 70%, and 50% of the peak velocities of A*j*. Fig. 7 shows the same type of results as Fig.6, but for the fling-step pulse-like ground motions B*j*. All the artificial non-pulse ground motions have identical peak accelerations equal to 0.2 g, and they have no velocity pulses that are in line with the proposed criteria for the selection of the near-fault pulse-like ground motions (see Section 2.1). In addition, the acceleration response spectra of the artificial non-pulse ground motions are consistent with those of the near-fault pulse-like ground motions, as shown in Figs. 8 and 9.

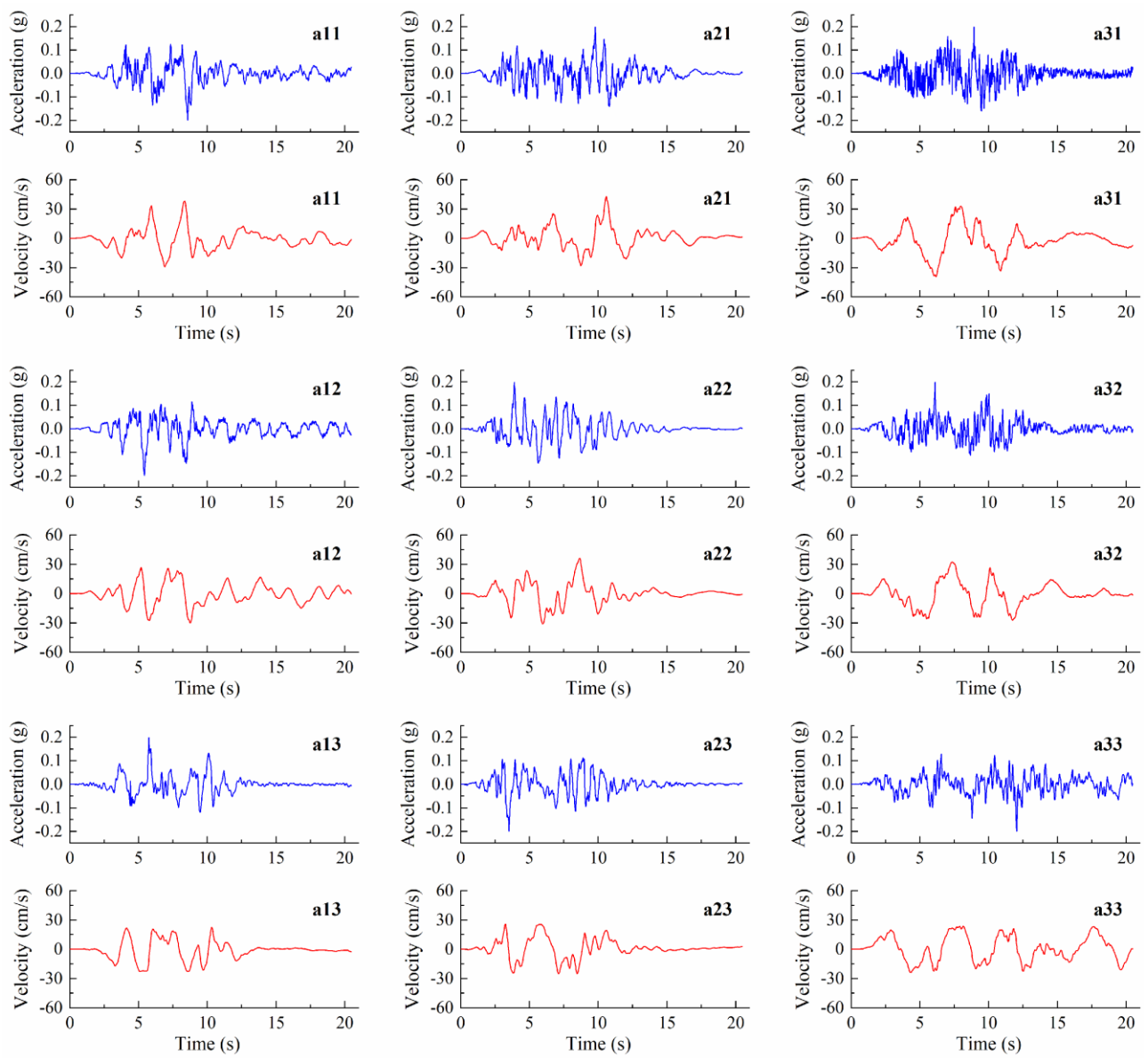


Fig. 6. Artificial non-pulse ground motions based on the forward-directivity pulse-like ground motions A1 (left column), A2 (middle column), and A3 (right column).

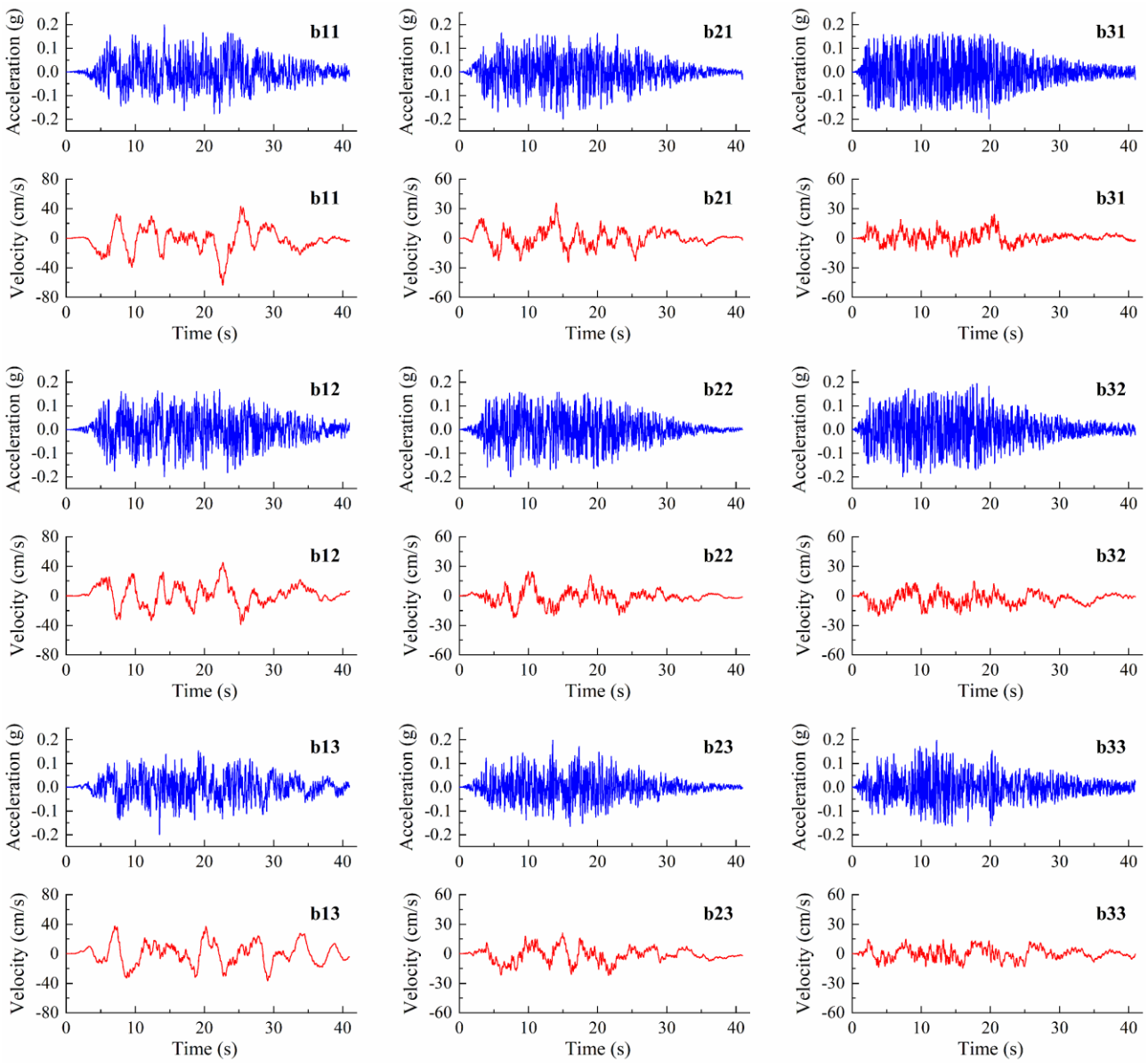


Fig. 7 Artificial non-pulse ground motions based on the fling-step pulse-like ground motions B1 (left column), B2 (middle column), and B3 (right column).

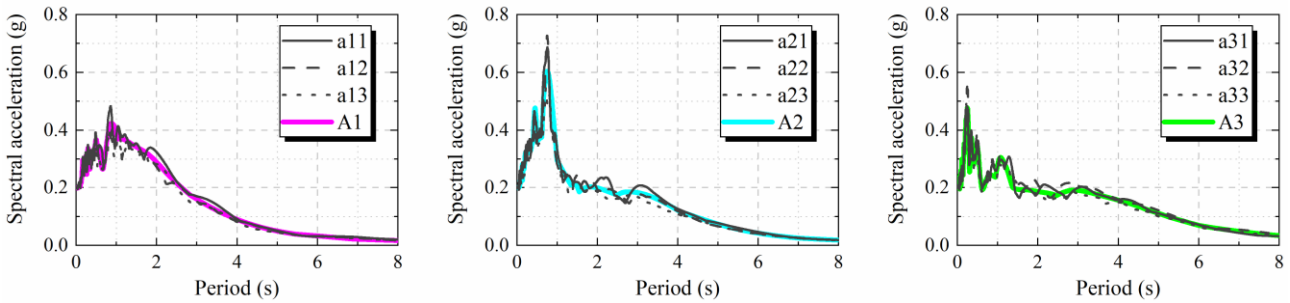


Fig. 8. Comparison of the spectral accelerations (5% damping) between the artificial non-pulse and forward-directivity pulse-like ground motions.

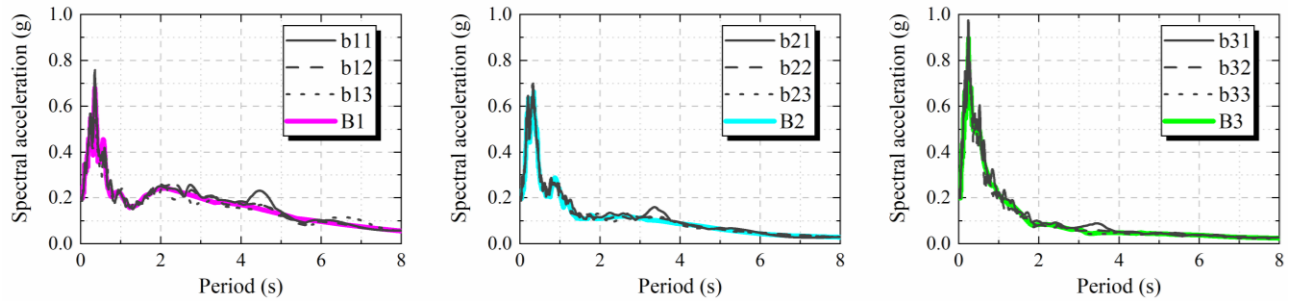


Fig. 9. Comparison of the spectral accelerations (5% damping) between the artificial non-pulse and fling-step pulse-like ground motions.

3. Numerical simulation and verification

A 2.5D FE-BE coupling method is employed to simulate the dynamic soil-tunnel interaction, which offers advantages for considering oblique incidence scenarios and the radiation damping effect. This section presents details of the hybrid numerical model and its verification.

3.1 Model parameters

The model of the considered soil-tunnel interaction system is illustrated in Fig. 1. The burial depth of the tunnel d = 20 m, and the outer radius of the tunnel r = 3.3 m. The thickness of the tunnel lining t = 0.35 m, and the tunnel lining has an elastic modulus E_t = 34.5 GPa, a mass density ρ_t = 2500 kg/m^3, a Poisson's ratio υ_t = 0.2, and a damping ratio ζ_t = 0.02. A perfect bonding condition between the tunnel and the surrounding soil applies, and a linear elastic behaviour for the tunnel is assumed.

The saturated soil is modelled as a two-phase medium based on Biot's theory of poroelasticity [42,43]. The governing equations of saturated poroelastic soil are expressed in the u-w formulation,

$$\mu u_{i,jj} + (\lambda + \alpha^2 M + \mu) u_{j,ji} + \alpha M w_{j,ji} = \rho \ddot{u}_i + \rho_f \ddot{w}_i \tag{1a}$$

$$\alpha M u_{j,ji} + M w_{j,ji} = \rho_f \ddot{u}_i + m \ddot{w}_i + b \dot{w}_i \tag{1b}$$

where u denotes the solid skeleton displacements and w denotes the relative displacements of the pore water to the solid skeleton; λ and μ are the Lame constants of the solid skeleton; $\rho = (1–n)\rho_s+n\rho_f$ is the mass density of the saturated soil, with ρ_s and ρ_f being the mass densities of the soil grain and pore water, respectively, and n being the porosity; α and M represent the compressibility of the soil grain

and pore water, respectively [44,45]; $m = (1+1/n)\rho_f/2n$ is a density-like parameter related to the inertial interaction of the solid skeleton and pore water [43,45]; $b = \rho_f g/k$ is a dissipative parameter related to the viscous interaction of the two phases, where g is the gravity acceleration, and k is the permeability [43,46].

Table 2
Material properties of the horizontally layered half-space.

Layer no.	Soil type	h (m)	μ_{max} (MPa)	ρ_s (kg/m^3)	υ_s	n	α	M (MPa)	m (kg/m^3)	b (N·s/m^4)
1	I	1	24.3	2518.2	0.43	0.45	0	0	0	0
2	I	4	24.3	2518.2	0.43	0.45	0.995	4551.7	3580.2	1.1×10^{10}
3	II	10	48.3	2304.8	0.43	0.35	0.991	5653.1	5510.2	2.8×10^{10}
4	III	12	111.2	2605.6	0.41	0.40	0.984	5049.5	4375.0	2.8×10^{10}
5	IV	12	254.1	2481.0	0.41	0.35	0.963	5677.7	5510.2	2.8×10^{8}
6	V	8	356.8	2507.1	0.41	0.35	0.984	5691.0	5510.2	5.6×10^{8}
7	VI	2	412.0	2650.0	0.42	0.40	0.932	5086.2	4375.0	1.4×10^{10}
8	V	8	451.7	2485.7	0.40	0.30	0.942	6485.5	7222.2	2.8×10^{8}
9	VI	12	367.6	2611.1	0.41	0.40	0.947	5076.0	4375.0	8.4×10^{9}
10	V	6	544.0	2600.0	0.42	0.30	0.911	6521.6	7222.2	5.6×10^{8}
11	VII	5	430.4	2566.7	0.41	0.40	0.938	5082.5	4375.0	2.8×10^{10}
Bedrock	-	Inf.	660.0	2542.9	0.42	-	-	-	-	-

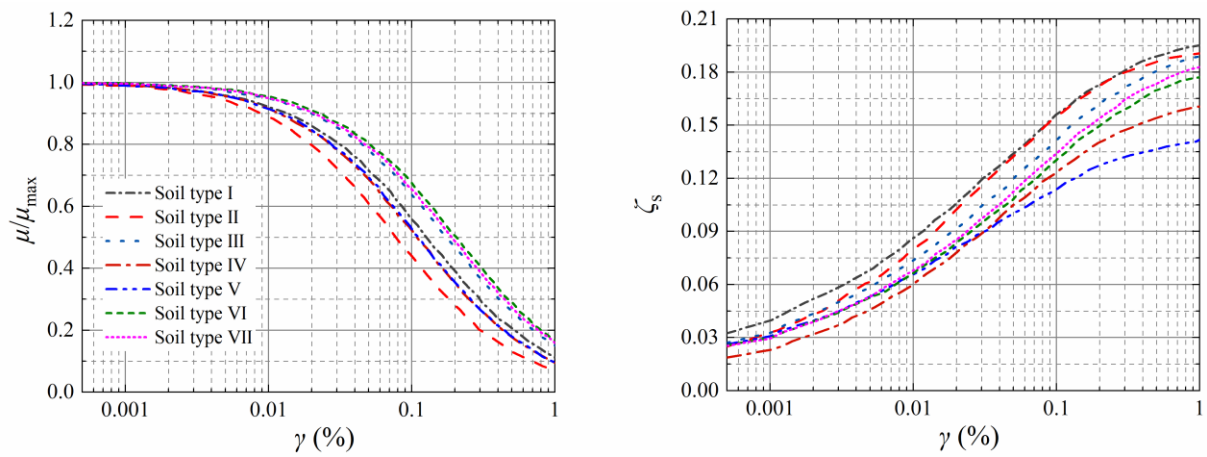


Fig. 10. Stiffness degradation and damping curves of the different types of soil.

Table 2 presents the material properties of the considered half-space, in which h denotes the thickness of each soil layer, μ_{max} denotes the shear modulus of the soil for small strains, and υ_s denotes

the Poisson's ratio. The first soil layer, which is above the groundwater level, is modelled as a dry poroelastic medium, and hence the parameters relating to the pore water are set to be zero; the soil layers below the groundwater level are modelled as saturated poroelastic media, with the mass density of the pore water ρ_f = 1000 kg/m^3; the bedrock is modelled as a non-porous medium, and the interface between the saturated soil layer and the bedrock is impermeable. The nonlinearity of the solid skeleton of the saturated poroelastic soil is considered by an equivalent linear approach. Fig. 10 shows the stiffness degradation and damping variations with the cyclic shear strain for the different types of soil. The considered stratigraphy is based on a field investigation of a typical saturated soil site in Tianjin, China, which mainly consists of clay and silty sand, and the stiffness degradation and damping curves are obtained from laboratory tests.

3.2 2.5D FE-BE modelling

Fig. 11 illustrates the 2.5D FE-BE hybrid model for this soil-tunnel system, which is considered longitudinally invariant, and thus its three-dimensional response for obliquely incident seismic waves can be obtained via a 2D mesh in the *x*-*o*-*z* plane with different wavenumbers in the *y*-direction, using Fourier transforms as follows.

$$\tilde{f}(x,k_y,z)=\frac{1}{2\pi}\int_{-\infty}^{+\infty} f(x,y,z)\exp(\mathrm{i}k_y y)\mathrm{d}y \tag{2a}$$

$$f(x,y,z)=\int_{-\infty}^{+\infty} \tilde{f}(x,k_y,z)\exp(-\mathrm{i}k_y y)\mathrm{d}k_y \tag{2b}$$

In this way, the computational effort is considerably reduced compared with a fully 3D model.

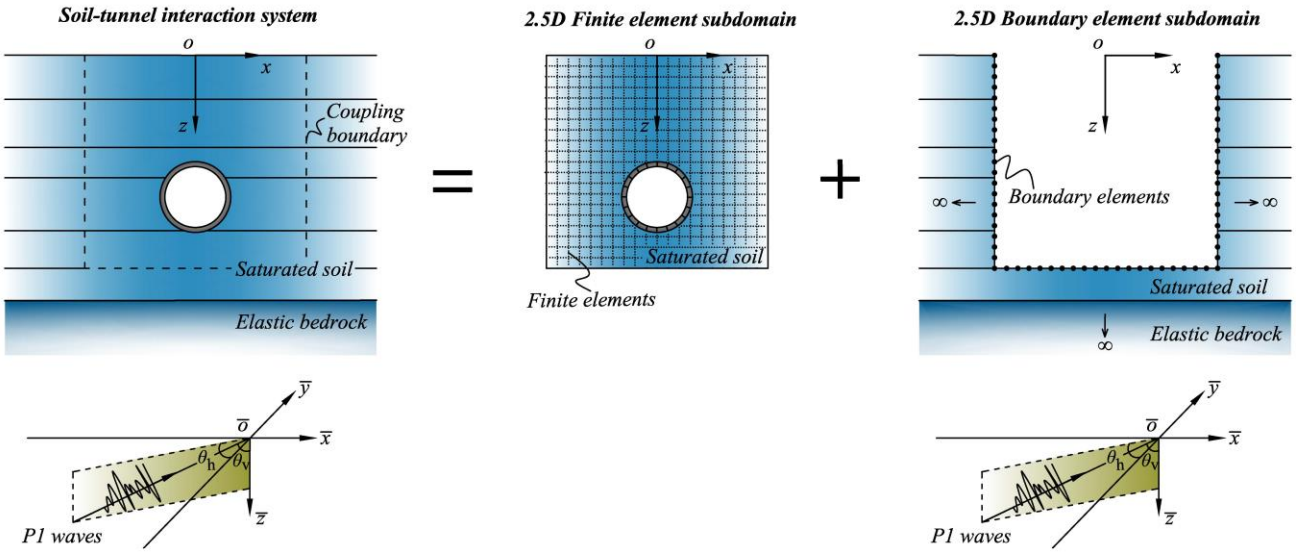


Fig. 11. The 2.5D finite element and boundary element hybrid model for a tunnel in a horizontally layered half-space with obliquely incident seismic waves.

The whole model is divided into two subdomains, namely, the FE subdomain consisting of the tunnel and the surrounding soil, and the BE subdomain corresponding to the unbounded soil region, including the bedrock. The FE subdomain is discretised with 2.5D two-phase elements [47] for the saturated poroelastic soil and 2.5D single-phase elements [48] for the tunnel lining. The 2.5D two-phase element has four nodes with six degrees of freedom per node, which are the displacements of the solid skeleton, u_x, u_y, and u_z, and the relative displacements of the pore water to the solid skeleton, w_x, w_y, and w_z. The 2.5D single-phase element also has four nodes but with three degrees of freedom per node, which are u_x, u_y, and u_z. The BE subdomain is discretised with two-node boundary elements along the interface of the two subdomains, and the nodes of the boundary elements overlap with those of the finite elements along the coupling boundary.

The seismic waves are obliquely incident from the elastic bedrock in the BE subdomain, while the FE subdomain is not subjected to external forces, with the ground motion transmitting into it through the coupling boundary. In the BE subdomain, the ground motion is a superposition of the free-field motion and scattered-field motion. The free-field motion caused by the obliquely incoming waves is obtained from analytical solutions [49] for the wave motion equation based on Biot's theory of poroelasticity (i.e., Eq. (1)). The scattered-field motion is due to the presence of the tunnel and is

irrespective of the angle of incidence, which is obtained by Green's functions for moving line loads in saturated poroelastic half-spaces [50]. The boundary element method can exactly satisfy the radiation condition at infinity and offers the advantage of allowing the simulation of scenarios of oblique angles of incidence.

The 2.5D FE-BE coupling method is implemented in the frequency domain, and the visco-elastic material behaviour of the soil and tunnel lining can be taken into account by replacing the Lame constants with their complex counterparts. The fast Fourier transform technique is used for the transformation between the frequency and time domains. First, the Fourier series of the input motion time history are obtained by the fast Fourier transform, and the amplitudes of the input motion in the frequency domain can be determined. Second, the transfer function of the soil-tunnel system (i.e., the ratio of the dynamic response to the input motion) is computed by the coupling method at the frequencies $f_m = m/(n\Delta t)$, where $m = 1, 2, \ldots, n/2$, n is the number of the recording points of the input motion time history, and Δt is the recording time step. Finally, the transfer function of the soil-tunnel system is multiplied by the Fourier series of the input motion, and the response of the soil-tunnel system in the time domain is obtained by the inverse fast Fourier transform.

The numerical simulation is conducted via a series of inhouse Fortran programs, as shown in Fig. 12. Soil nonlinearity is considered by two equivalent linear processes. First, an equivalent linear site response analysis of the horizontally layered half-space is performed by a stiffness matrix method [51], incorporating an iterative procedure to update the material properties of each soil layer with its shear strain. The shear moduli and damping ratios compatible with the soil shear strains are used as the input parameters for the BE subdomain to account for the soil nonlinearity in the far field, which is assumed to be identical to a free-field scenario. As for the soil nonlinearity in the near field (i.e., the FE subdomain), it may be different from that for the free-field scenario, due to the soil-tunnel interaction. To this end, an element-level equivalent linear process is further conducted in the FE subdomain in the subsequent coupling computation to consider the non-uniform degradation of soil stiffness around

the tunnel. The convergence of the equivalent linear analysis in the FE subdomain is achieved when the differences in the shear strain of each soil finite element between two successive iterations fall below a predetermined tolerance (e.g., 0.05 is adopted in this study). It should be noted that the size of the FE subdomain depends on the equivalent linear behaviour of the soil around the tunnel, which will be discussed in detail in Section 3.3.

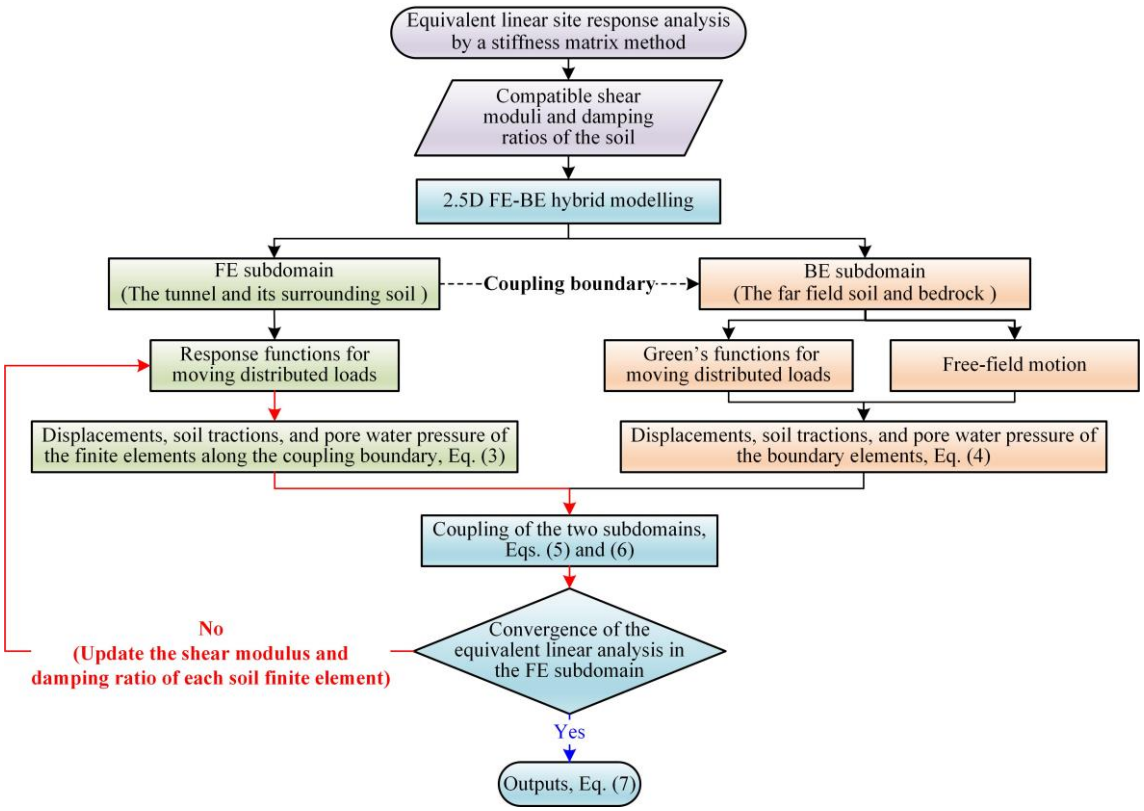


Fig. 12. Flow chart of the 2.5D FE-BE hybrid modelling incorporating equivalent linear analysis.

The 2.5D FE-BE hybrid modelling is an application of the authors' previous efforts in numerical simulation of the soil-tunnel interaction for obliquely incident seismic waves. The methodology is well described in [47], which will be briefly introduced here for the sake of completeness. In the FE subdomain, the displacement, soil traction, and pore water pressure response of the *i*-th coupled finite element are expressed as,

$$u_i^1 = \sum_{j=1}^{N} r_{ij}^u q_j^1 \quad (i = 1, 2, ..., N) \tag{3a}$$

$$w_i^1 = \sum_{j=1}^{N} r_{ij}^w q_j^1 \quad (i = 1, 2, ..., N) \tag{3b}$$

$$t_i^1 = \sum_{j=1}^{N} r_{ij}^t q_j^1 \quad (i = 1, 2, ..., N) \tag{3c}$$

$$p_i^1 = \sum_{j=1}^{N} r_{ij}^p q_j^1 \quad (i = 1, 2, ..., N) \tag{3d}$$

where r_{ij}^u, r_{ij}^w, r_{ij}^t, and r_{ij}^p are the response functions for the solid skeleton displacements, pore water relative displacements, soil tractions, and pore water pressure, respectively, q_j^1 is the unknown traction acting on the *j*-th finite element along the coupling boundary, and *N* is the number of the coupled finite elements. The response functions can be determined from the element average response of the solid skeleton displacements, pore water relative displacements, soil tractions, and pore water pressure induced by unit moving line loads acting on each finite element along the coupling boundary. In the BE subdomain, the displacement, soil traction, and pore water pressure response of the *i*-th boundary element are expressed as,

$$u_i^2 = \sum_{j=1}^{N} g_{ij}^u q_j^2 + u_i^f \quad (i = 1, 2, ..., N) \tag{4a}$$

$$w_i^2 = \sum_{j=1}^{N} g_{ij}^w q_j^2 + w_i^f \quad (i = 1, 2, ..., N) \tag{4b}$$

$$t_i^2 = \sum_{j=1}^{N} g_{ij}^t q_j^2 + t_i^f \quad (i = 1, 2, ..., N) \tag{4c}$$

$$p_i^2 = \sum_{j=1}^{N} g_{ij}^p q_j^2 + p_i^f \quad (i = 1, 2, ..., N) \tag{4d}$$

where g_{ij}^u, g_{ij}^w, g_{ij}^t, and g_{ij}^p are the Green's functions for the solid skeleton displacements, pore water relative displacements, soil tractions, and pore water pressure, respectively, q_j^2 is the unknown traction acting on the *j*-th boundary element, and u_i^f, w_i^f, t_i^f, and p_i^f denote the free-field response of the solid skeleton displacements, pore water relative displacements, soil tractions, and pore water

pressure, respectively.

The key procedure of the coupling of the two subdomains is to solve the unknown tractions along the coupling boundary, namely, q_j^1 and q_j^2. The FE and BE subdomains are coupled through the displacement compatibility and stress (soil tractions and pore water pressure) equilibrium conditions along the coupling boundary,

$$\mathbf{u}_j^1 = \mathbf{u}_j^2 \quad \text{and} \quad w_{nj}^1 = w_{nj}^2 \qquad (j = 1,2,\cdots,N) \tag{5a}$$

$$\mathbf{t}_j^1 + \mathbf{t}_j^2 = 0 \quad \text{and} \quad p_j^1 + p_j^2 = 0 \qquad (j = 1,2,\cdots,N) \tag{5b}$$

in which the superscripts "1 and 2" denote the finite elements and boundary elements, respectively, and w_n represents the pore water relative displacement normal to the coupling boundary. The unknown tractions can be obtained from the coupling equation,

$$\begin{bmatrix} -\mathbf{R}_u & \mathbf{G}_u \\ -\mathbf{R}_{wn} & \mathbf{G}_{wn} \\ \mathbf{R}_t & \mathbf{G}_t \\ \mathbf{R}_p & \mathbf{G}_p \end{bmatrix} \begin{Bmatrix} \mathbf{q}^1 \\ \mathbf{q}^2 \end{Bmatrix} = -\begin{Bmatrix} \mathbf{u}^f \\ \mathbf{w}_n^f \\ \mathbf{t}^f \\ \mathbf{p}^f \end{Bmatrix} \tag{6}$$

in which $\mathbf{R}_u$, $\mathbf{R}_{wn}$, $\mathbf{R}_t$, $\mathbf{R}_p$, $\mathbf{G}_u$, $\mathbf{G}_{wn}$, $\mathbf{G}_t$, and $\mathbf{G}_p$ are fully populated matrices collecting the abovementioned response functions and Green's functions, respectively.

Finally, the nodal displacements of the FE mesh can be obtained by substituting the load vector $\mathbf{q}^1$ into the finite element equation,

$$\begin{bmatrix} \mathbf{K}_{\mathrm{ii}} & \mathbf{K}_{\mathrm{ic}} \\ \mathbf{K}_{\mathrm{ci}} & \mathbf{K}_{\mathrm{cc}} \end{bmatrix} \begin{Bmatrix} \mathbf{U}_{\mathrm{i}} \\ \mathbf{U}_{\mathrm{c}} \end{Bmatrix} = \begin{Bmatrix} \mathbf{o} \\ \mathbf{A}\mathbf{q}^1 \end{Bmatrix} \tag{7}$$

where the subscripts "c and i" denote the nodes along the coupling boundary and the interior nodes of the FE subdomain, respectively, and the tractions are transformed into equivalent nodal forces through the transformation matrix **A**.

3.3 Verification

The validity and accuracy of the 2.5D FE-BE hybrid modelling incorporating equivalent linear analysis are verified with two examples: (1) the equivalent linear site response obtained by the 2.5D FE-BE coupling method is compared with that by a finite element simulation in PLAXIS v22.01 [52] to demonstrate the correctness for simulating wave propagation in a saturated poroelastic half-space; (2) a sensitivity analysis is conducted to determine the size of the FE subdomain for simulating the soil-tunnel interaction.

3.3.1 Equivalent linear site response

Two cases of site response are considered: a saturated poroelastic soil site and a dry soil site. The two sites have the same material properties as those in Table 2 and Fig. 10, while for the dry soil site case (i.e., a single-phase medium), parameters relating to the pore water are set to zero. The fling-step pulse-like ground motion B1 is chosen as the input motion, and the horizontal and vertical angles of incidence are $\theta_h = 90°$ and $\theta_v = 0°$, i.e., a vertical incidence scenario which is critical for the coupling effect of the solid skeleton and pore water. To employ the 2.5D FE-BE coupling method, a FE subdomain of height $H = 30$ m and width $L = 28$ m is adopted. Note that, for this free-field exercise, the size of the FE subdomain would not affect the results. The length of the finite elements and boundary elements is at least 10 times smaller than the minimum shear-wave length that is of interest in the simulation, resulting in 1168 elements in the FE subdomain with 104 elements along the coupling boundary, as shown in Fig. 13.

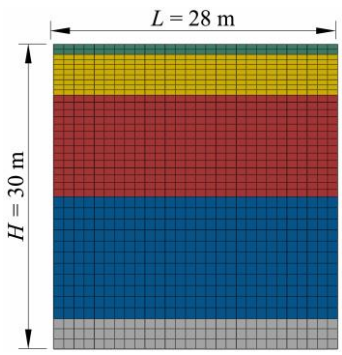


Fig. 13. The mesh of the FE subdomain for the free-field case.

For the PLAXIS finite element simulation, the compatible shear moduli and damping ratios of the soil, resulting from the stiffness matrix method, are employed to simulate the equivalent linear site response, and the viscous damping is introduced by the Rayleigh formulation. The ground surface acceleration at the center point of the FE mesh by the 2.5D FE-BE coupling method is compared with that resulting by the PLAXIS finite element simulation. Figs. 14 and 15 show the comparison between the two methods for the saturated poroelastic and dry soil sites, respectively. The slight differences in the acceleration response spectra between the two methods can be attributed to the numerical dissipation of high frequencies due to the Newmark time-integration scheme ($\beta_{dyn} = 0.3025$, $\gamma_{dyn} = 0.6$) adopted in the PLAXIS analysis [53]. Moreover, the two methods employ different formulations for the saturated poroelastic soil; the FE-BE coupling method adopts a *u-w* formulation, while a *u-p* formulation is used in PLAXIS, which may also explain the slight differences observed for the saturated poroelastic soil site case.

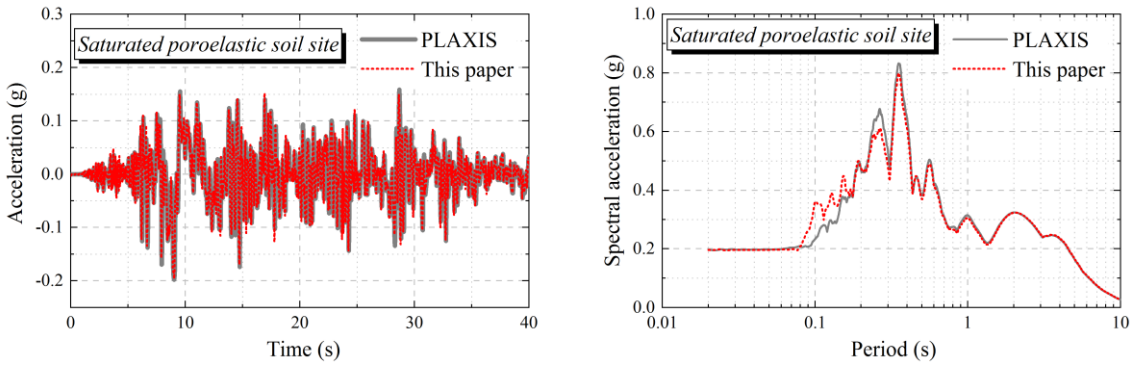


Fig. 14. Comparison of the ground surface acceleration of the saturated poroelastic soil site between PLAXIS and this paper for the fling-step pulse-like ground motion B1 with $\theta_h = 90°$ and $\theta_v = 0°$.

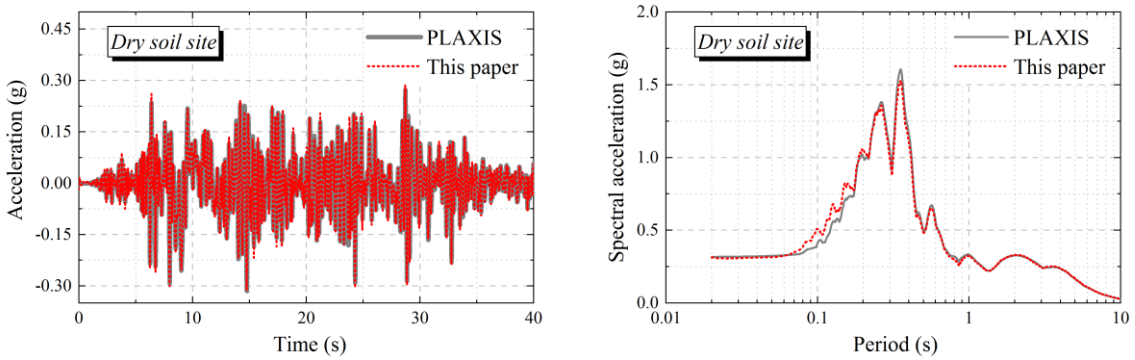


Fig. 15. Comparison of the ground surface acceleration of the dry soil site between PLAXIS and this paper for the fling-step pulse-like ground motion B1 with $\theta_h = 90°$ and $\theta_v = 0°$.

It is noteworthy that there are noticeable differences in the ground surface acceleration between the saturated poroelastic and dry soil site cases, as shown in Figs. 14 and 15. For this exercise, the peak ground acceleration of the saturated poroelastic soil site is significantly smaller than that of the dry soil site, and the differences in the spectral accelerations are prominent in the period range of 1 s. This highlights the influence of the pore water on the seismic site response, which can further affect the seismic tunnel response. It is therefore necessary to investigate the seismic response characteristics of the tunnel in saturated poroelastic soil for near-fault pulse-like ground motions.

3.3.2 Soil-tunnel interaction

As discussed in Section 3.2, the presence of the tunnel may affect the soil shear strains around it. Therefore, when it comes to the soil-tunnel interaction scenario, the size of the FE subdomain should be larger than the affected area to ensure that the soil equivalent linear behaviour in the BE subdomain equals the free-field scenario. Concerning the soil-tunnel system described in Section 3.1, four FE subdomain models are tested. As shown in Fig. 16, The four FE subdomain models have the same height H = 30 m while different widths L = 10, 16, 28, and 40 m. The soil medium of the four FE subdomain models is discretised into 1498, 1798, 2398, and 2998 elements, respectively, while the tunnel lining is discretised into 240 elements, with 3 elements in the radial direction and 80 elements along the circumference.

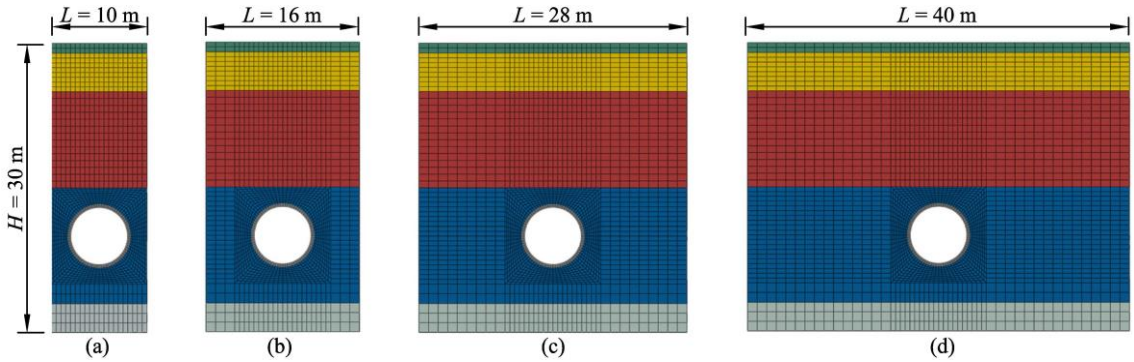


Fig. 16. The mesh of the FE subdomain with different widths for the soil-tunnel system.

Fig. 17 shows the distribution of the peak soil shear strains in the FE subdomain for the forward-directivity pulse-like ground motion A1 with θ_h = 45° and θ_v = 45°. Fig. 18 presents the peak shear strain profiles at the boundaries of the different FE subdomain models and along the tunnel center, as well as the peak shear strain profile for the free field case. Larger soil shear strains occur around the tunnel, and the maximum soil shear strains are concentrated in the soft soil layer and right above the tunnel, indicating the influence of soil-tunnel interaction. However, the affected area seems to be rather limited, this is because the flexibility ratio [54] $F = E_s r^3 (1-\nu_t^2) / 6E_t I_t (1+\nu_s)$ = 10 for the considered soil-tunnel system, which means that the soil is much stiffer than the tunnel, and hence the soil tends to restrict the tunnel deformation. The magnitude of the soil shear strains stabilises when the width of the FE subdomain is larger than 28 m, and the free-field response is recovered at the boundary of the FE subdomain model with the width L = 28 m, suggesting that it is sufficiently large to account for the influence of the tunnel on the soil shear strain. It is worth mentioning that although the sensitivity analysis considers only the oblique incidence case of θ_h = 45° and θ_v = 45°, the determined size of the FE subdomain is applicable to arbitrary angles of incidence for the soil-tunnel system, as the obliquely incident P1 waves with θ_h = 45° and θ_v = 45° result in the most significant shear deformation in the soil, which will be discussed in Section 4.2.

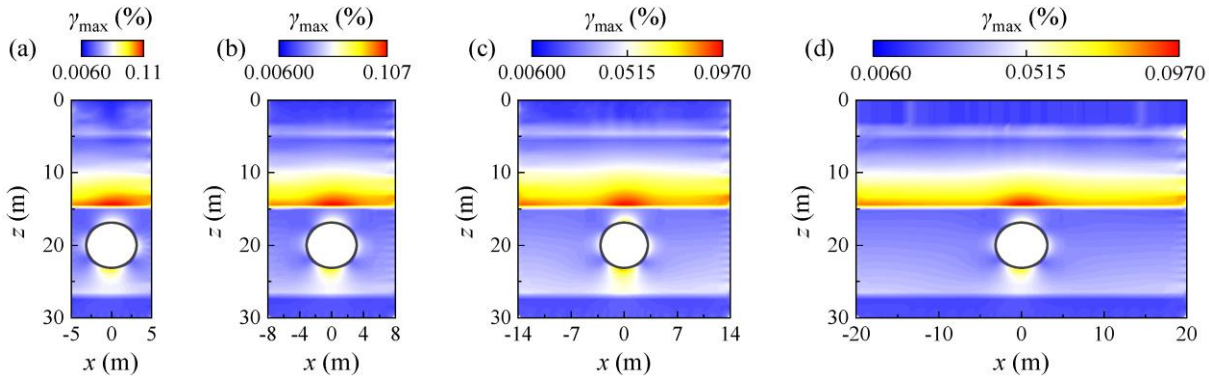


Fig. 17. Peak soil shear strains for the forward-directivity pulse-like ground motion A1 with θ_h = 45° and θ_v = 45°, and for the FE subdomain with (a) L = 10 m, (b) L = 16 m, (c) L = 28 m, and (d) L = 40 m.

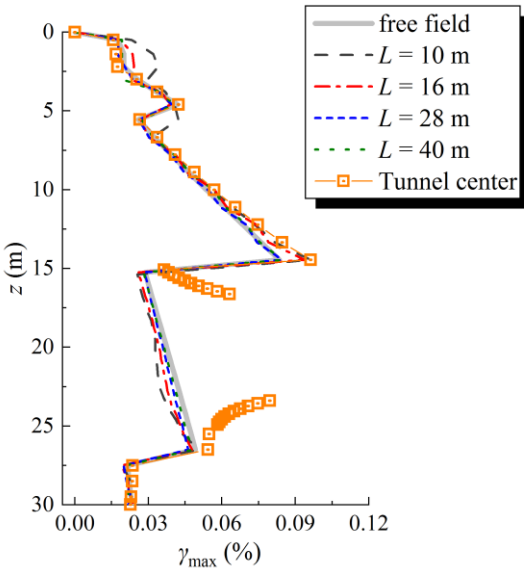


Fig. 18. Peak shear strain profiles for the forward-directivity pulse-like ground motion A1 with $\theta_h = 45°$ and $\theta_v = 45°$: the solid grey line represents the free-field response; the lines for L = 10, 16, 28, and 40 m represent peak shear strain profiles of the soil column at the boundaries of the different FE subdomain models for the soil-tunnel system; the line for the tunnel center represents the peak shear strain profile of the soil column at x = 0 m.

To investigated the influence of the size of the FE subdomain on the tunnel internal forces, Fig. 19 compares the envelopes of the transverse bending moment and axial force of the tunnel lining for the different FE subdomain models, and Fig. 20 compares the time histories of the longitudinal bending moment and axial force of the tunnel lining. It should be noted that the tunnel lining is modelled as a linear elastic material. Therefore, such a simplification may lead to an overestimation of the tunnel internal forces if the lining experiences plastic deformation or cracking [25,55]. The influence of the size of the FE subdomain on the tunnel internal forces is minor. Only slight differences in the transverse bending moment (Fig. 19(a)) and longitudinal bending moment (Fig. 20(a)) can be found between the small FE subdomain model (i.e., L = 10 m) and the larger ones. Based on the foregoing analysis, the FE subdomain with L = 28 m is adopted for the following computation.

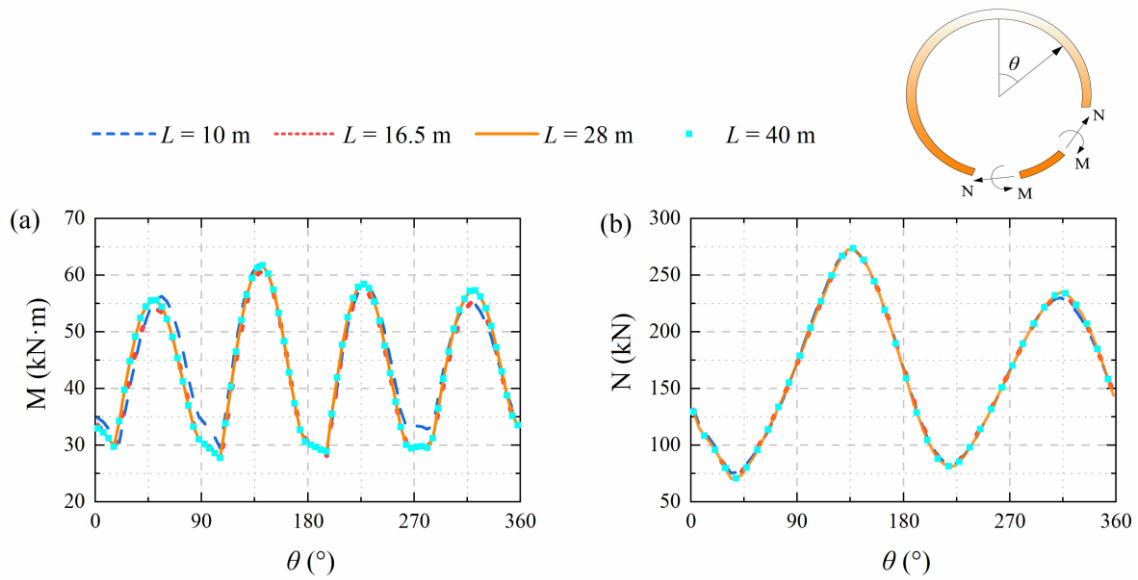


Fig. 19. Envelopes of the transverse (a) bending moment M and (b) axial force N of the tunnel lining for the forward-directivity pulse-like ground motion A1 with θ_h = 45° and θ_v = 45°, and for the different FE subdomain models.

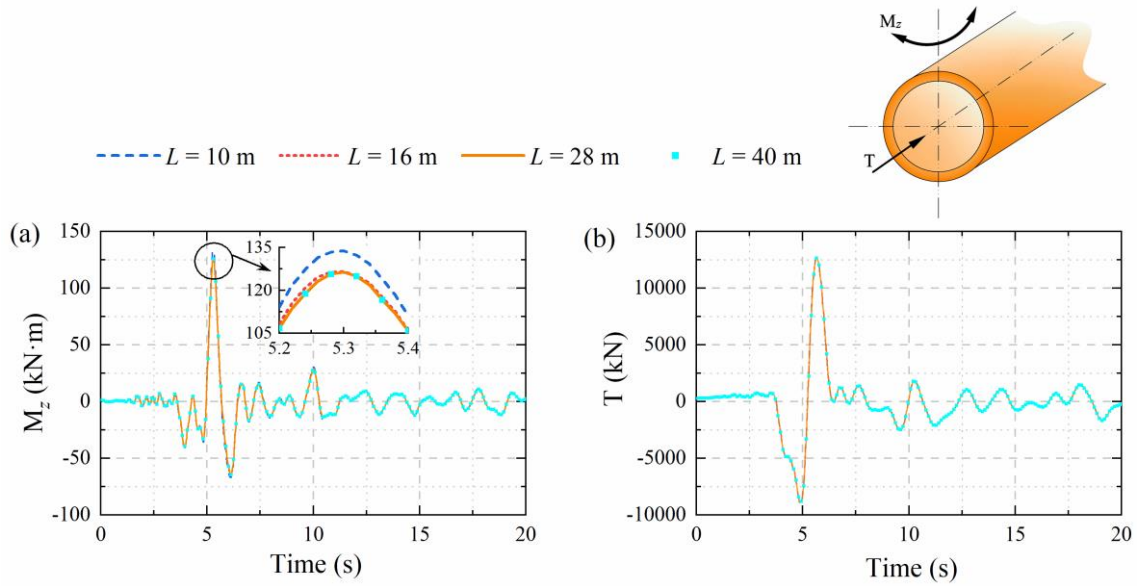


Fig. 20. Time histories of the longitudinal (a) bending moment M_z and (b) axial force T of the tunnel lining for the forward-directivity pulse-like ground motion A1 with θ_h = 45° and θ_v = 45°, and for the different FE subdomain models.

4. Results and analysis

The seismic tunnel response for obliquely incident near-fault pulse-like waves is investigated via two levels in this section, to gain insight into the effects of the velocity pulses. First, comparison of the tunnel internal forces between the selected near-fault pulse-like and far-fault ground motions are presented to show the overall influence of the near-fault pulse-like ground motions. Then, the effects

of the two types of velocity pulses (i.e., forward-directivity and fling-step velocity pulses) are further investigated by comparisons of the tunnel internal forces, soil shear strains, and seismic pore water pressure between the near-fault pulse-like and artificial non-pulse ground motions.

4.1 Comparison between the near-fault pulse-like and far-fault ground motions

The selected forward-directivity pulse-like, fling-step pulse-like, and far-fault ground motions in Table 1 are employed as the input motions, with the horizontal angle of incidence θ_h = 45° and the vertical angle of incidence θ_v = 0°, 30°, 45°, 60°, 80°. Fig. 21 shows the tunnel internal forces for the three types of ground motions, in which plots (a) and (b) show the maximum transverse bending moment (M) and axial force (N) in the tunnel lining, and plots (c) and (d) show the peak values of the time histories of the longitudinal bending moment (M_z) and axial force (T). Note that, for the vertical incidence case (i.e., θ_v = 0°), seismic waves arrive simultaneously along the longitudinal direction, and hence the longitudinal bending moment and axial force of the tunnel equal zero. The magnitude of the tunnel internal forces is a function of the vertical angle of incidence. The dispersion of the results for the different input motions is more significant for larger vertical angles of incidence, and this is more pronounced for the near-fault pulse-like ground motions than the far-fault ground motions. For the vertical incidence case, the differences in the transverse bending moment and transverse axial force between the near-fault pulse-like and far-fault ground motions are quite small, suggesting a minor influence of the velocity pulses. The transverse bending moment, transverse axial force, and longitudinal bending moment are the largest for the forward-directivity pulse-like ground motion A1 with θ_v = 45°, 30°, and 60°, respectively, while the longitudinal axial force T is the largest for the fling-step pulse-like ground motion B1 with θ_v = 60°. It is worth mentioning that the fling-step pulse-like ground motion B1 has the largest peak velocity among the selected ground motions.

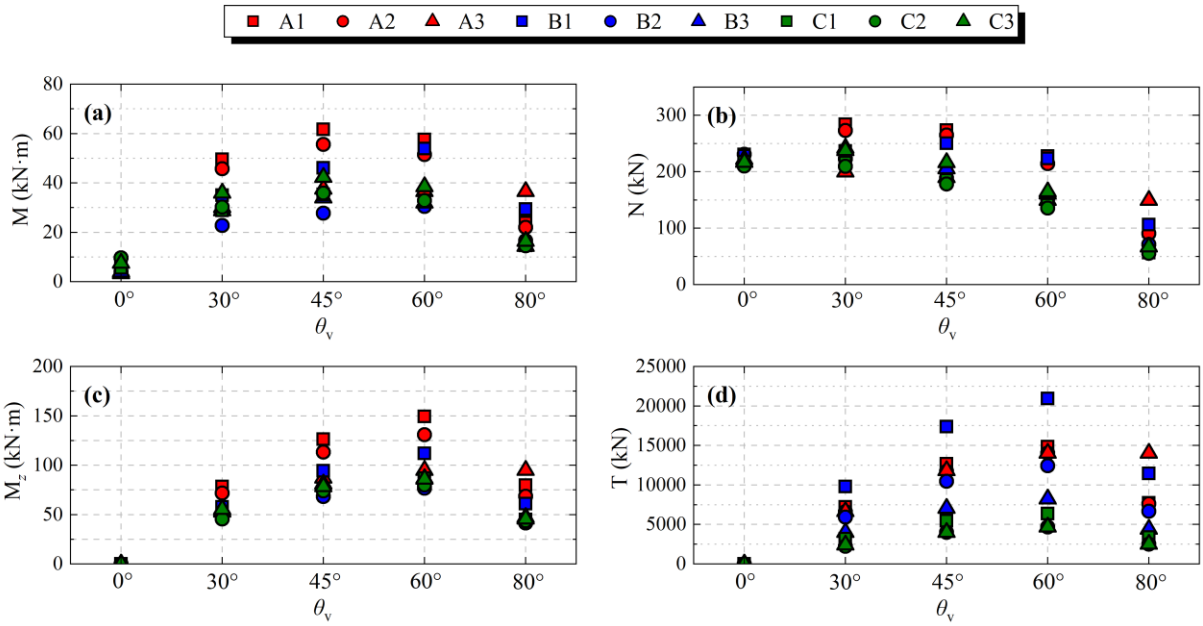


Fig. 21. The (a) transverse bending moment, (b) transverse axial force, (c) longitudinal bending moment, and (d) longitudinal axial force of the tunnel lining for the forward-directivity pulse-like ground motions (A1, A2, and A3), fling-step pulse-like ground motions (B1, B2, and B3), and far-fault ground motions (C1, C2, and C3).

Fig. 22 compares the mean values of the tunnel internal forces for the three types of ground motions. The near-fault pulse-like ground motions generally cause larger tunnel internal forces compared to the far-fault ground motions. The forward-directivity pulse-like ground motions result in the largest mean values of the tunnel internal forces, with the exception of the transverse bending moment for the vertical incidence case. The differences in the tunnel internal forces between the fling-step pulse-like and far-fault ground motions are smaller. Like the forward-directivity pulse-like ground motions, the fling-step pulse-like ground motions may result in smaller transverse bending moment than the far-fault ground motions for small vertical angles of incidence. It seems that the amplification effect of the near-fault pulse-like ground motions on the tunnel internal forces is more prominent for the forward-directivity pulse-like ground motions and for large vertical angles of incidence. However, this effect is associated not only with the velocity pulses of the near-fault pulse-like ground motions but also with their spectral characteristics, as the acceleration response spectra of the two types of pulse-like ground motions are distinctly different (see Fig. 5). To identify the contribution of the velocity pulses, the influence of the spectral characteristics should be excluded, and we will further

discuss this issue in the next section.

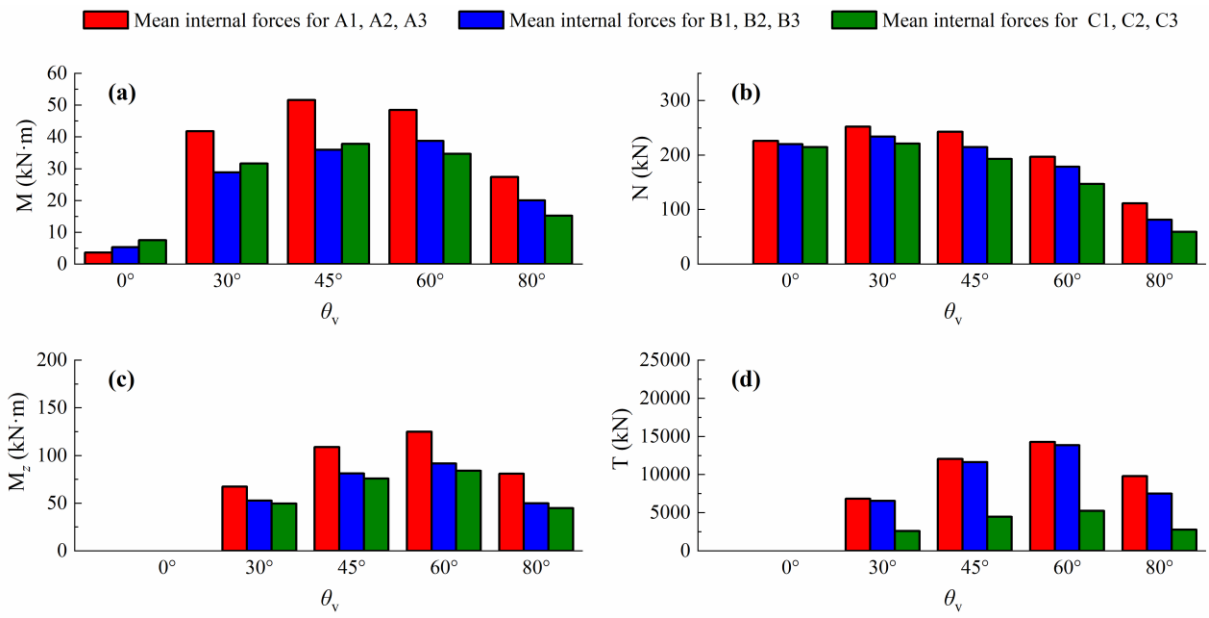


Fig. 22. Comparison of the mean values of (a) transverse bending moment, (b) transverse axial force, (c) longitudinal bending moment, and (d) longitudinal axial force of the tunnel lining for the forward-directivity pulse-like ground motions (A1, A2, and A3), fling-step pulse-like ground motions (B1, B2, and B3), and far-fault ground motions (C1, C2, and C3).

Fig. 22(d) also shows that the increase in the longitudinal axial force induced by the near-fault pulse-like ground motions are noticeably larger than the other internal forces. Table 3 summarises the percentage differences in the mean values of the tunnel internal forces between the near-fault pulse-like and far-fault ground motions. The differences in the tunnel internal forces between the near-fault pulse-like and far-fault ground motions tend to increase with the vertical angle of incidence, and the differences for the forward-directivity pulse-like ground motions are considerably larger than those for the fling-step pulse-like ground motions. The differences in the transverse bending moment, transverse axial force, and longitudinal bending moment for the forward-directivity pulse-like ground motions can reach and exceed 80%, while the differences in the longitudinal axial force T are always significantly larger than 160% and can be up to 251% for the vertical angle of incidence $\theta_v = 80°$.

Table 3
Percentage differences (%) in the mean values of the tunnel internal forces between the near-fault pulse-like and far-fault ground motions.

θ_v	M		N		M_z		T	
	FD	FS	FD	FS	FD	FS	FD	FS
0°	-51	-29	5	3	-	-	-	-
30°	32	-9	14	6	36	6	162	152
45°	36	-5	26	11	43	7	169	159
60°	40	12	34	21	49	9	173	165
80°	80	32	88	37	81	12	251	169

Note: FD denotes forward-directivity pulse-like ground motions, and FS denotes fling-step pulse-like ground motions.

4.2 Effects of the velocity pulses

The comparison of the seismic tunnel response between the near-fault pulse-like and far-fault ground motions indicates that the near-fault pulse-like ground motions can cause noticeable amplification in the tunnel internal forces, but this effect is a consequence of the interaction of the velocity pulses and the spectral characteristics. To identify the contribution of the velocity pulses, a comparative study on the seismic tunnel response between the near-fault pulse-like ground motions and the artificial non-pulse ground motions, which have consistent acceleration response spectra with the near-fault pulse-like ground motions (see Figs 8 and 9), is conducted in this section. In Fig. 23, r_{ij} (i, j = 1, 2, 3) represents the ratios of the maximum tunnel internal forces for the forward-directivity pulse-like ground motions (Ai) to those for the artificial non-pulse ground motions (aij), and R_M, R_N, R_{Mz}, and R_T denote the transverse bending moment ratio, transverse axial force ratio, longitudinal bending moment ratio, and longitudinal axial force ratio, respectively. Most of the internal force ratios are larger than unity, although their magnitude varies significantly for the different ground motions and is affected by the vertical angle of incidence. This indicates that the forward-directivity velocity pulse has a tendency to increase the tunnel internal forces, noting that the acceleration response spectra of the artificial non-pulse ground motions are consistent with those of the forward-directivity pulse-like ground motions. It is therefore evident that the increases in the tunnel internal forces can be attributed to the forward-directivity velocity pulse. However, the artificial non-pulse ground motions

a31, a32, and a33 may lead to larger transverse bending moments and axial forces in the tunnel lining than the forward-directivity pulse-like ground motion A3, due to the stochastic nature of the ground motions. Although the artificial non-pulse ground motions have similar spectral characteristics in terms of the acceleration response spectra compared to the near-fault pulse-like ground motions, the frequency content of the artificial non-pulse and near-fault pulse-like ground motions is not identical, which may explain the internal force ratios less than unity.

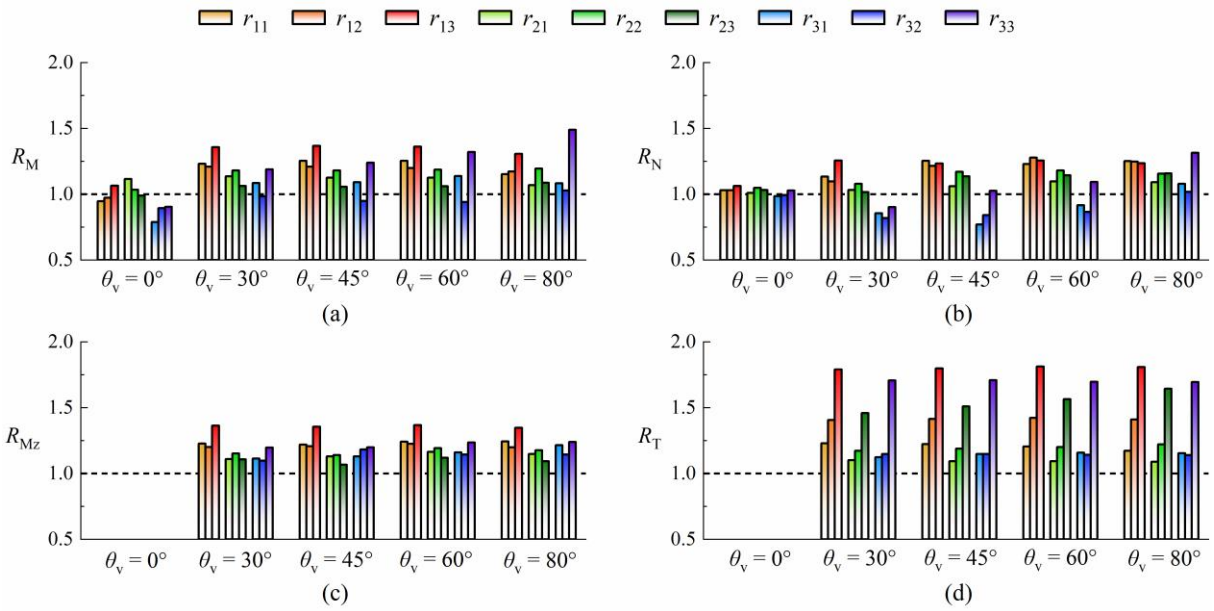


Fig. 23. Ratios of the maximum (a) transverse bending moment, (b) transverse axial force, (c) longitudinal bending moment, and (d) longitudinal axial force of the tunnel lining for the forward-directivity pulse-like ground motions to those for the artificial non-pulse ground motions.

Fig. 24 shows the same type of results as Fig. 23, but for the fling-step pulse-like ground motions, in which r_{ij} (i, j = 1, 2, 3) represents the ratios of the maximum tunnel internal forces for the fling-step pulse-like ground motions (Bi) to those for the artificial non-pulse ground motions (bij). The fling-step velocity pulse can also lead to noticeable increases in the tunnel internal forces. As shown in Figs. 23 and 24, the transverse bending moment ratio R_M, transverse axial force ratio R_N, and longitudinal bending moment ratio R_{Mz} may be less than unity due to the stochastic nature of the artificial non-pulse ground motions, while the longitudinal axial force ratio R_T is always larger than unity, suggesting that the longitudinal axial force is more sensitive to the velocity pulses. Moreover, the longitudinal axial

force ratio R_T tends to be larger for the artificial non-pulse ground motions with smaller peak velocities, noting that the peak velocities of the artificial non-pulse ground motions a*j*1, a*j*2, and a*j*3 (b*j*1, b*j*2, and b*j*3) are, respectively, about 90%, 70%, and 50% of the peak velocities of the near-fault pulse-like ground motions A*j* (B*j*). The latter indicates that the peak velocity is a critical factor that affects the magnitude of the longitudinal axial force.

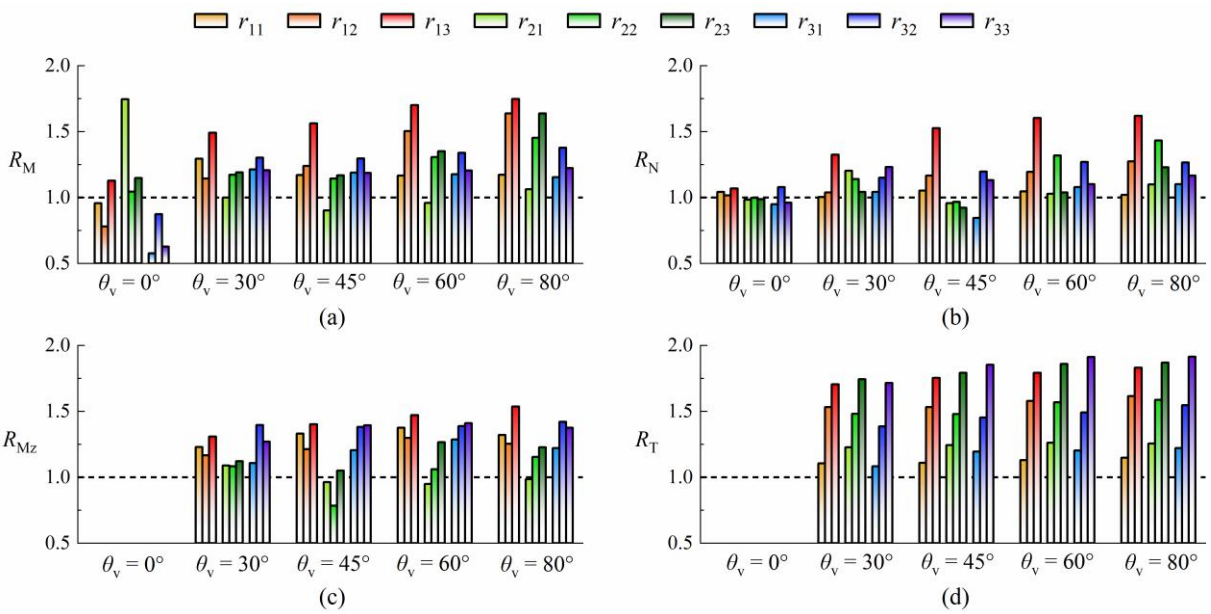


Fig. 24. Ratios of the maximum (a) transverse bending moment, (b) transverse axial force, (c) longitudinal bending moment, and (d) longitudinal axial force of the tunnel lining for the fling-step pulse-like ground motions to those for the artificial non-pulse ground motions.

To compare the effects of the two types of velocity pulses, the percentage differences between the tunnel internal forces for the pulse-like ground motions and the average values of the tunnel internal forces for the corresponding three artificial non-pulse ground motions are calculated. Tables 4 and 5 present the differences for the forward-directivity and fling-step pulse-like ground motions, respectively. Like the results in Table 3, namely, the percentage differences in the tunnel internal forces between the near-fault pulse-like and far-fault ground motions, the amplification effect of the pulse-like ground motions is larger for large vertical angles of incidence. However, comparison of Table 4 and Table 5 suggests that when the acceleration response spectra are similar, the fling-step velocity pulse can lead to more significant increases in the tunnel internal forces than the forward-directivity

velocity pulse, as the differences in the tunnel internal forces between the forward-directivity pulse-like and artificial non-pulse ground motions are generally smaller than those between the fling-step pulse-like and artificial non-pulse ground motions. This is contrary to the results in Table 3.

Table 4
Percentage differences (%) in the tunnel internal forces between the forward-directivity pulse-like and artificial non-pulse ground motions.

θ_v	M			N			M_z			T		
	A1	A2	A3	A1	A2	A3	A1	A2	A3	A1	A2	A3
0°	0	5	-14	4	3	0	-	-	-	-	-	-
30°	27	13	9	16	4	-14	26	12	14	47	24	33
45°	28	12	9	23	12	-12	26	11	17	48	26	34
60°	27	13	13	25	14	-4	28	16	18	48	29	33
80°	21	12	20	25	14	14	26	14	20	48	32	33

Table 5
Percentage differences (%) in the tunnel internal forces between the fling-step pulse-like and artificial non-pulse ground motions.

θ_v	M			N			M_z			T		
	B1	B2	B3	B1	B2	B3	B1	B2	B3	B1	B2	B3
0°	-4	31	-31	4	-1	0	-	-	-	-	-	-
30°	31	12	24	12	13	14	23	10	26	45	48	39
45°	32	7	22	25	-5	6	32	-7	33	47	51	50
60°	46	12	24	28	13	15	38	9	36	50	56	54
80°	52	38	25	30	25	18	37	12	34	53	57	56

Fig. 25 shows the distribution of peak soil shear stains for the forward-directivity pulse-like ground motions and the artificial non-pulse ground motions, with $\theta_h = 45°$ and $\theta_v = 45°$ as an example. Fig. 26 shows the same type of results as Fig. 25, but for the fling-step pulse-like ground motions and the artificial non-pulse ground motions. Comparison of the results between the near-fault pulse-like and artificial non-pulse ground motions indicates that the velocity pulses would not change the soil shear deformation pattern, as large soil shear strains always occur in the soft soil layer and right above the tunnel. Nevertheless, it has a big influence on the magnitude of the soil shear strains. Fig. 27 presents the ratios of the maximum soil shear stains for the near-fault pulse-like ground motions to the corresponding ones for the artificial non-pulse ground motions. In general, the soil shear strains are larger for the near-fault pulse-like ground motions, which is also observed in the shaking table tests by

Yang et al. [32], while exceptions may occur due to variations in the frequency content of the artificial non-pulse ground motions.

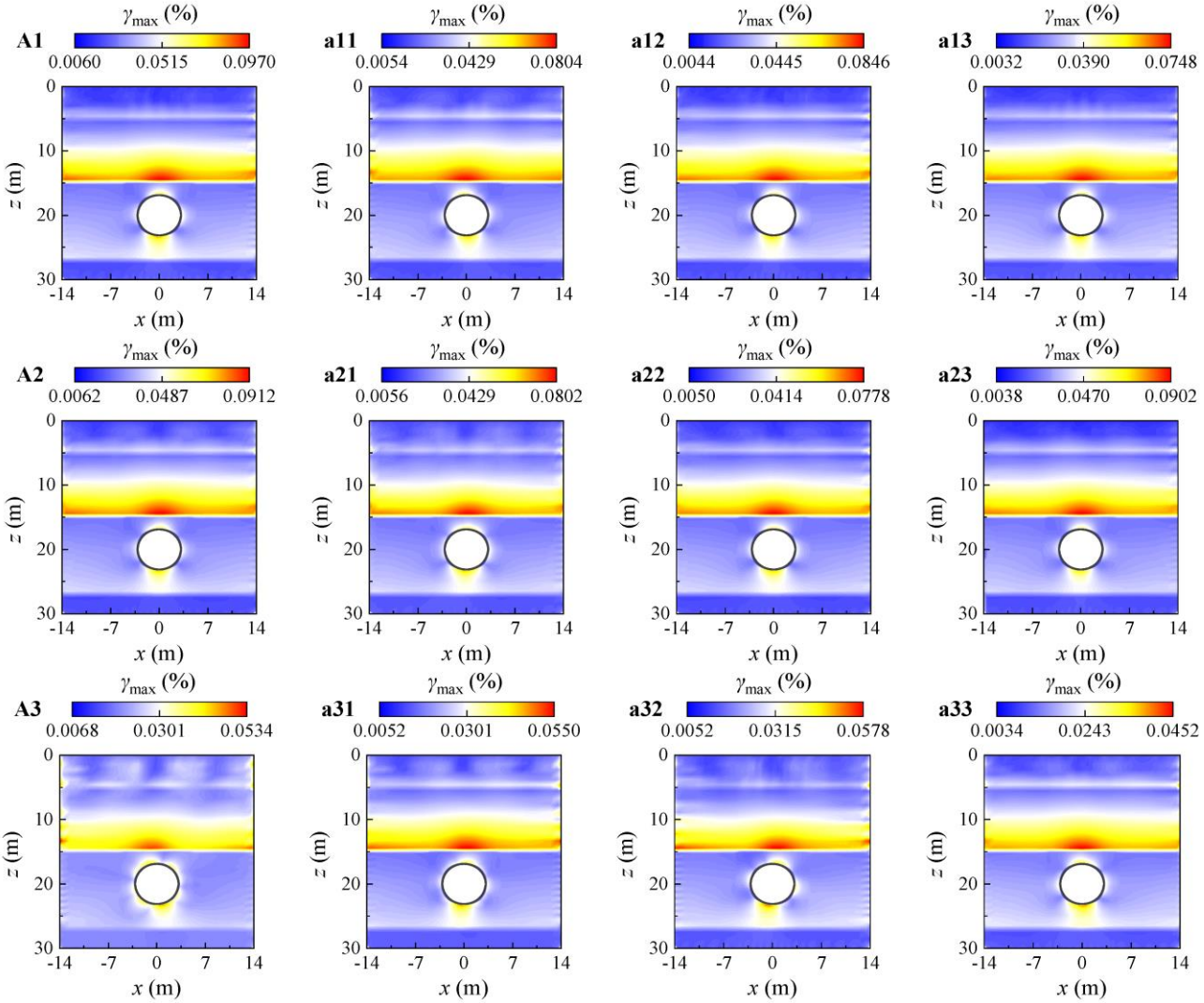


Fig. 25. Peak soil shear stains for the forward-directivity pulse-like ground motions (A1, A2, and A3) and the artificial non-pulse ground motions (a11, a12, a13; a21, a22, a23; a31, a32, a33), with θ_h = 45° and θ_v = 45°.

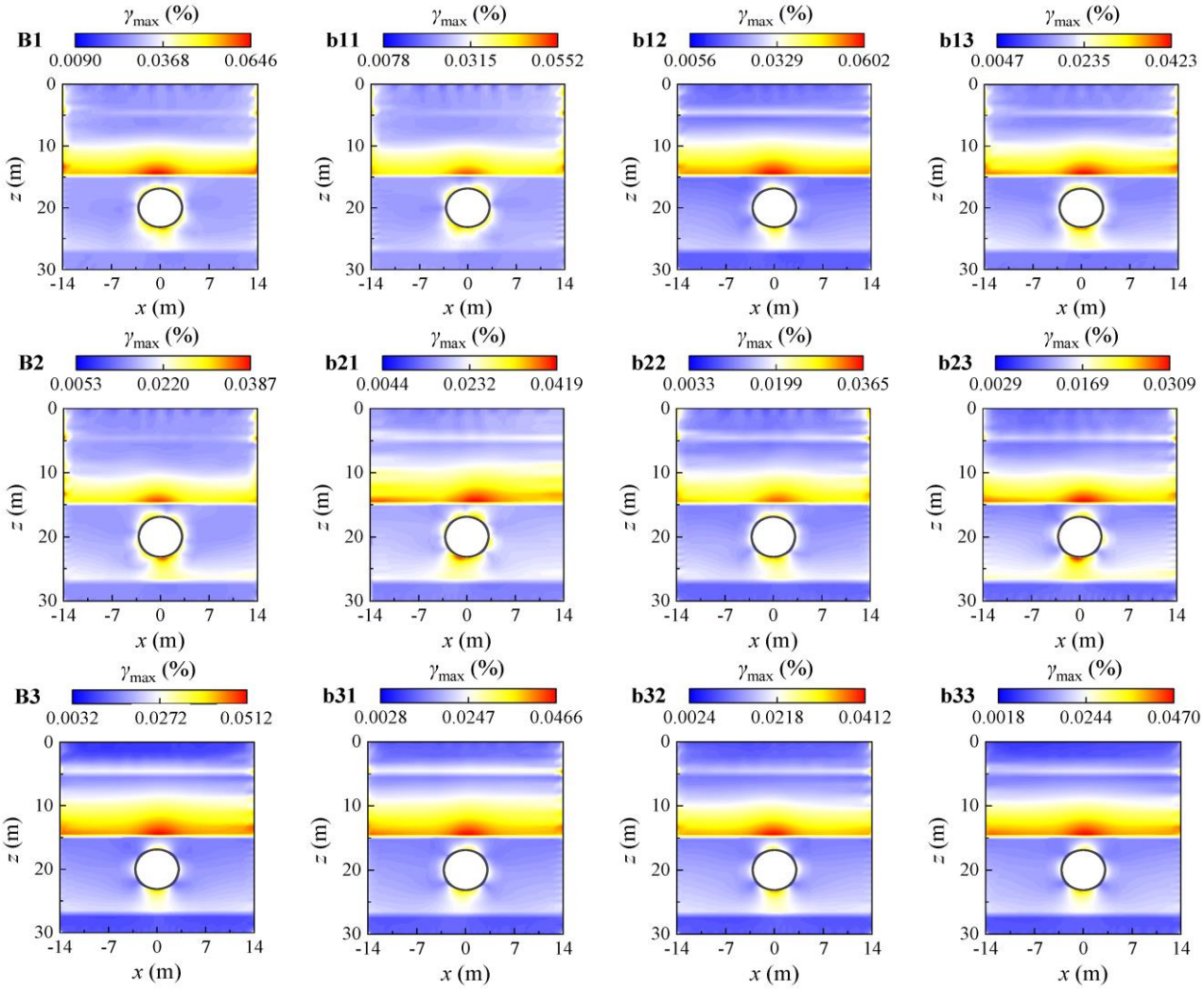


Fig. 26. Peak soil shear stains for the fling-step pulse-like ground motions (B1, B2, and B3) and the artificial non-pulse ground motions (b11, b12, b13; b21, b22, b23; b31, b32, b33), with θ_h = 45° and θ_v = 45°.

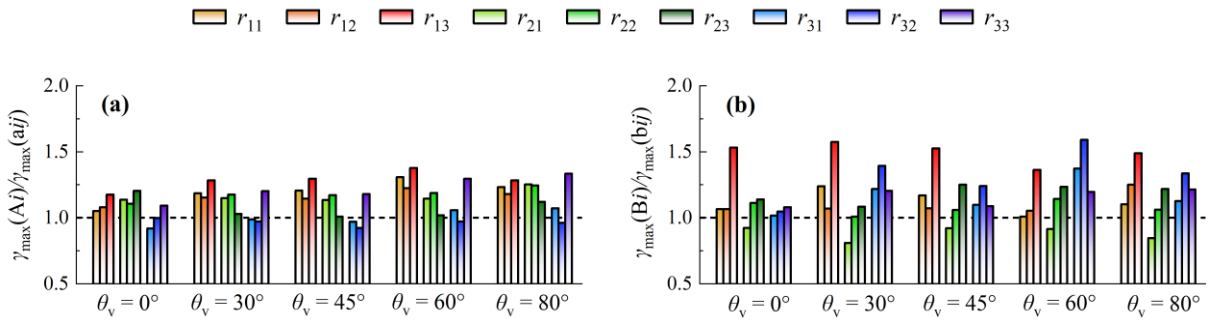


Fig. 27. (a) Ratios of the maximum soil shear stains for the forward-directivity pulse-like ground motions to those for the artificial non-pulse ground motions, and (b) ratios of the maximum soil shear stains for the fling-step pulse-like ground motions to those for the artificial non-pulse ground motions.

Fig. 28 shows the distribution of peak seismic pore water pressure for the forward-directivity pulse-like ground motions and the artificial non-pulse ground motions, with θ_h = 45° and θ_v = 45° as an example. Fig. 29 shows the same type of results as Fig. 28, but for the fling-step pulse-like ground

motions and the artificial non-pulse ground motions. The seismic pore water pressure tends to increase with the depth. Fig. 30 presents the ratios of the peak seismic pore water pressure at the bottom of the tunnel for the near-fault pulse-like ground motions to the corresponding ones for the artificial non-pulse ground motions. For a vertical angle of incidence, the differences in the seismic pore water pressure ratios for the different artificial non-pulse ground motions are noticeable. As discussed earlier, this can most likely be attributed to the stochastic nature of the artificial non-pulse ground motions. In addition, for a near-fault pulse-like ground motion, the seismic pore water pressure ratios tend to increase with the vertical angle of incidence, which is more significant for the fling-step pulse-like ground motions.

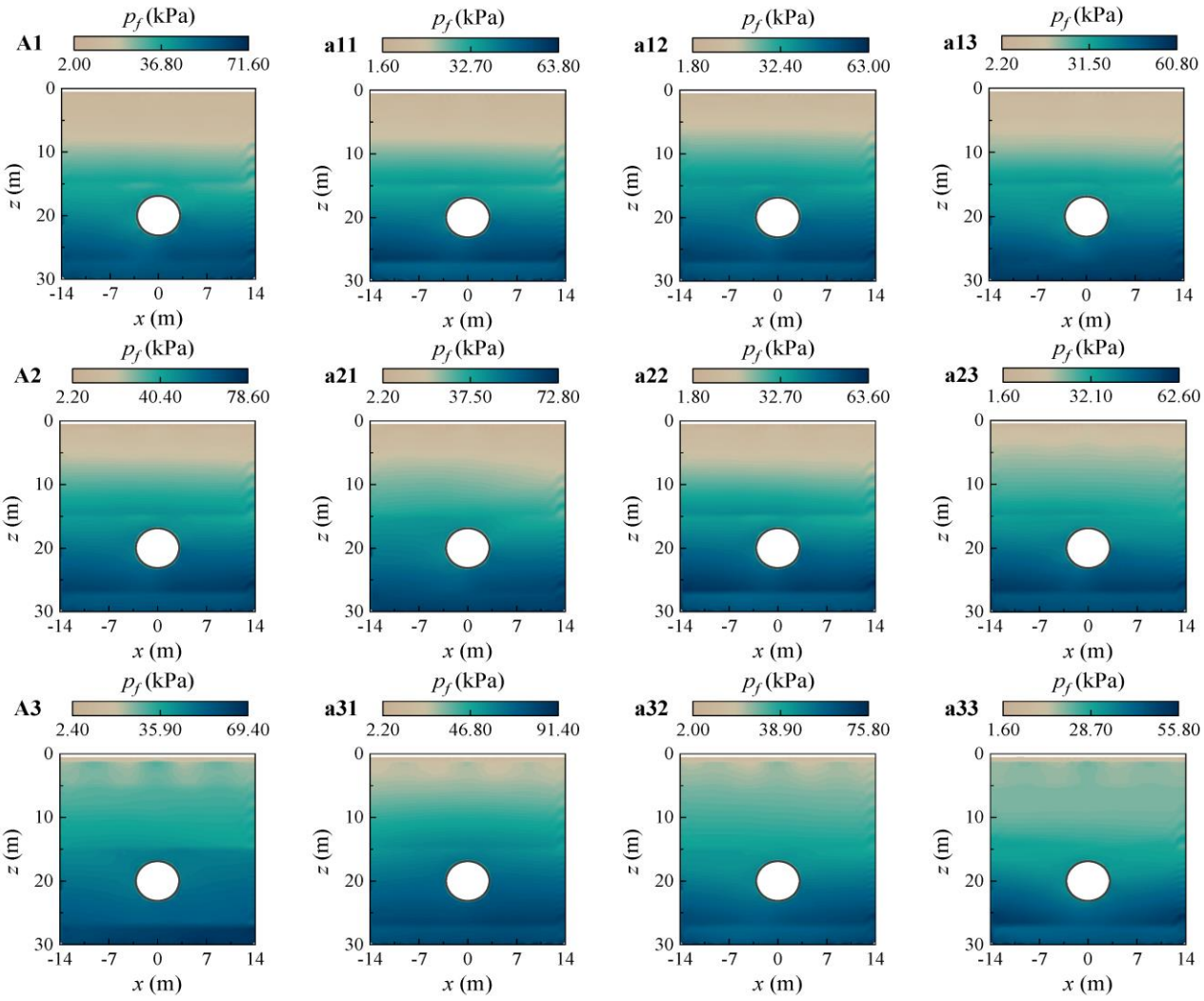


Fig. 28. Peak seismic pore water pressure for the forward-directivity pulse-like ground motions (A1, A2, and A3) and the artificial non-pulse ground motions (a11, a12, a13; a21, a22, a23; a31, a32, a33), with $\theta_h = 45°$ and $\theta_v = 45°$.

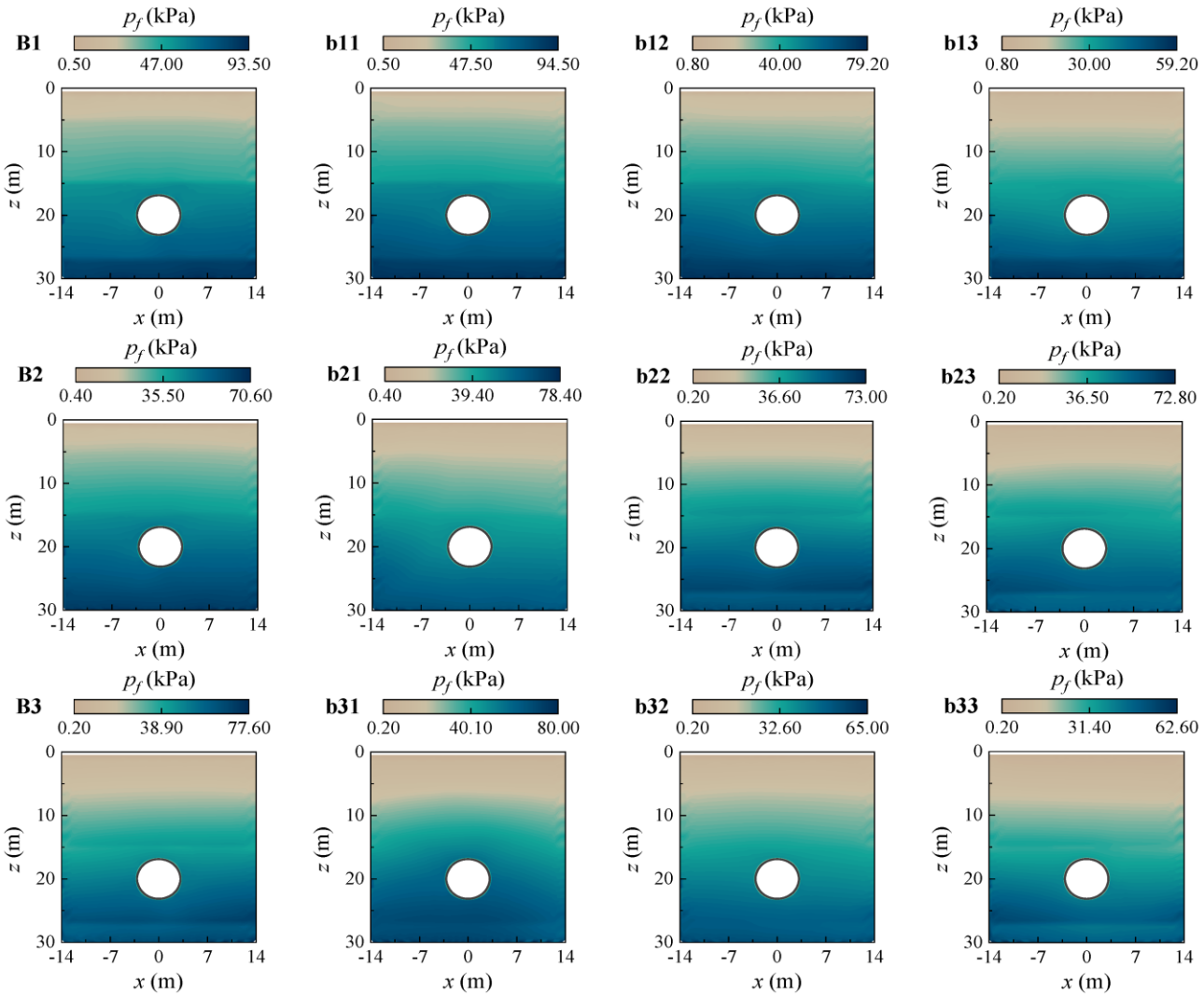


Fig. 29. Peak seismic pore water pressure for the fling-step pulse-like ground motions (B1, B2, and B3) and the artificial non-pulse ground motions (b11, b12, b13; b21, b22, b23; b31, b32, b33), with $\theta_h = 45°$ and $\theta_v = 45°$.

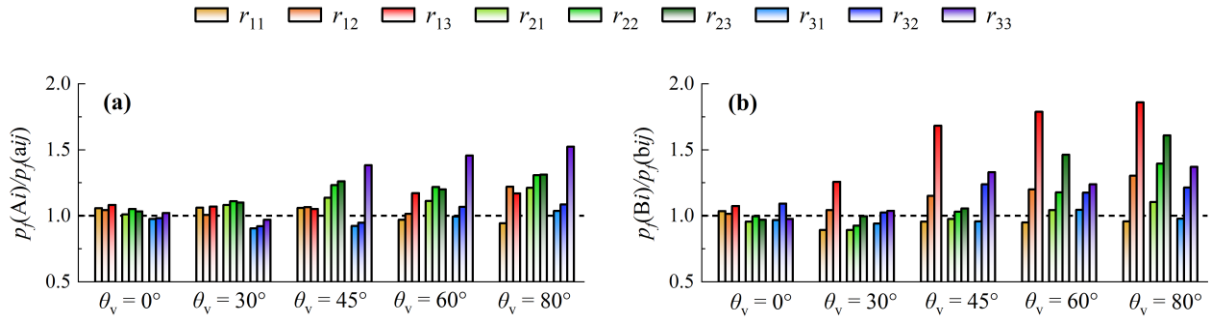


Fig. 30. (a) Ratios of the peak seismic pore water pressure for the forward-directivity pulse-like ground motions to those for the artificial non-pulse ground motions, and (b) ratios of the peak seismic pore water pressure for the fling-step pulse-like ground motions to those for the artificial non-pulse ground motions.

5. Summary and conclusions

This study numerically investigates the effects of the near-fault pulse-like ground motions on the seismic response of a tunnel in saturated poroelastic soil, with P1 waves obliquely incident from the elastic bedrock. The solution to this dynamic soil-tunnel interaction is a 2.5D FE-BE coupling method, and the longitudinal tunnel response due to the wave passage effect is considered. The principal findings are as follows.

1. The near-fault pulse-like ground motions have a tendency to cause larger tunnel internal forces than the far-fault ground motions. For the selected ground motions in this study, this amplification effect is more significant for the forward-directivity pulse-like ground motions than the fling-step pulse-like ones. However, this is a consequence of the interaction of the velocity pulses and the spectral characteristics of the near-fault pulse-like ground motions. The comparison of the tunnel internal forces between the near-fault pulse-like and artificial non-pulse ground motions indicates that, for pulse-like ground motions with similar acceleration response spectra, the fling-step velocity pulse can be more detrimental to the tunnel than the forward-directivity velocity pulse.
2. The angle of incidence has a big influence on the seismic tunnel response. The magnitude of the tunnel internal forces is more dispersed for the different near-fault pulse-like ground motions with larger vertical angles of incidence. Moreover, the amplification effect of the near-fault pulse-like ground motions on the tunnel internal forces is more significant for larger vertical angles of incidence.
3. The longitudinal axial force of the tunnel lining is more sensitive to the velocity pulses than the other internal forces (i.e., the transverse bending moment and axial force and the longitudinal bending moment). The pulse-like ground motions may cause considerably large longitudinal axial forces in the lining, and the magnitude tends to increase with the peak ground velocity.
4. The velocity pulses would not change the soil shear deformation pattern, but it may increase the

magnitude of the soil shear strain. For large vertical angles of incidence, the velocity pulses may significantly amplify the seismic pore water pressure around the tunnel, and the effect is more pronounced for the fling-step velocity pulse.

This study investigates the effects of near-fault pulse-like ground motions on the seismic tunnel response for an oblique incidence scenario, with the emphasis placed on identifying and distinguishing the influence of the two types of velocity pulses. A limited number of representative near-fault pulse-like and far-fault ground motions are considered. Further research on this topic, involving a larger number of ground motion records, is of interest to gain a more comprehensive understanding of the effects of the velocity pulses. In addition, the soil nonlinearity is approximated by an equivalent linear approach with visco-elastic constitutive models, and the tunnel is assumed to behave in a linear elastic fashion. More advanced constitutive models, e.g., elasto-plastic constitutive models, are needed to account for the nonlinear behaviour more rigorously.

Acknowledgements

This study was supported by the National Natural Science Foundation of China under Grants 52008013, 52192675, and 51978462, which are gratefully acknowledged.

References

[1] Argani LP, Gajo A. A novel insight into vertical ground motion modelling in earthquake engineering. International Journal for Numerical and Analytical Methods in Geomechanics 2022;46(1):164-186. http://doi.org/10.1002/nag.3295

[2] Abrahamson NA, Somerville PG. Effects of the hanging wall and footwall on ground motions recorded during the Northridge earthquake. Bulletin of the Seismological Society of America 1996;86:S93-S99. https://doi.org/10.1785/BSSA08601B0S93

[3] Baker JW. Quantitative classification of near-fault ground motions using wavelet analysis. Bulletin of the Seismological Society of America 2007;97:1486-1501. http://doi.org/10.1785/0120060255

[4] Bray JD, Rodriguez-Marek A. Characterization of forward-directivity ground motions in the near-fault region. Soil Dynamics and Earthquake Engineering 2004;24:815-828. http://doi.org/10.1016/j.soildyn.2004.05.001

[5] Mavroeidis GP, Papageorgiou AS. A mathematical representation of near-fault ground motions. Bulletin of the Seismological Society of America 2003;93:1099-1131. https://doi.org/10.1785/0120020100

[6] Mukhopadhyay S, Gupta VK. Directivity pulses in near-fault ground motions-I: Identification, extraction and

modeling. Soil Dynamics and Earthquake Engineering 2013;50:1-15. http://doi.org/10.1016/j.soildyn.2013.02.017

[7] Shahi SK, Baker JW. An efficient algorithm to identify strong-velocity pulses in multicomponent ground motions. Bulletin of the Seismological Society of America 2014;104:2456-2466. http://doi.org/10.1785/0120130191

[8] Somerville PG, Smith NF, Graves RW, Abrahamson NA. Modification of empirical strong ground motion attenuation relations to include the amplitude and duration effects of rupture directivity. Seismological Research Letters 1997;68:199-222. https://doi.org/10.1785/gssrl.68.1.199

[9] Wang GQ, Zhou XY, Zhang PZ, Igel H. Characteristics of amplitude and duration for near fault strong ground motion from the 1999 Chi-Chi, Taiwan earthquake. Soil Dynamics and Earthquake Engineering 2002;22(1):73-96. https://doi.org/10.1016/S0267-7261(01)00047-1

[10] Housner GW, Hudson DE. The Port Hueneme earthquake of March 18, 1957. Bulletin of the Seismological Society of America 1958;48(2):163-168. https://doi.org/10.1785/BSSA0480020163

[11] Bertero VV, Mahin SA, Herrera RA. Aseismic design implications of near-fault San Fernando earthquake records. Earthquake Engineering & Structural Dynamics 1978;6(1):31-42. https://doi.org/10.1002/eqe.4290060105

[12] Hall JF, Heaton TH, Halling MW, Wald DJ. Near-source ground motion and its effects on flexible buildings. Earthquake Spectra 1995;11:569-605. https://doi.org/10.1193/1.1585

[13] Hatzigeorgiou GD. Behavior factors for nonlinear structures subjected to multiple near-fault earthquakes. Computers & Structures 2010;88:309-321. http://doi.org/10.1016/j.compstruc.2009.11.006

[14] Sasani M, Bertero VV. Importance of severe pulse-type ground motions in performance-based engineering: Historical and critical review. Proceedings of the 12th World Conference on Earthquake Engineering, New Zealand Society for Earthquake Engineering, Upper Hutt, New Zealand, 2000.

[15] Kalkan E, Kunnath SK. Assessment of current nonlinear static procedures for seismic evaluation of buildings. Engineering Structures 2007;29(3):305-316. https://doi.org/10.1016/j.engstruct.2006.04.012

[16] Kalkan E, Kunnath SK. Effects of fling step and forward directivity on seismic response of buildings. Earthquake Spectra 2006;22:367-390. http://doi.org/10.1193/1.2192560

[17] Alavi B, Krawinkler H. Behavior of moment-resisting frame structures subjected to near-fault ground motions. Earthquake Engineering & Structural Dynamics 2004;33:687-706. http://doi.org/10.1002/eqe.369

[18] Dong H, Han Q, Du X, Liu J. Constant ductility inelastic displacement ratios for the design of self-centering structures with flag-shaped model subjected to pulse-type ground motions. Soil Dynamics and Earthquake Engineering 2020;133:106143. http://doi.org/10.1016/j.soildyn.2020.106143

[19] Sehhati R, Rodriguez-Marek A, ElGawady M, Cofer WF. Effects of near-fault ground motions and equivalent pulses on multi-story structures. Engineering Structures 2011;33:767-779. http://doi.org/10.1016/j.engstruct.2010.11.032

[20] Xu W, Luo Z, Yan W, Chen Y, Wang J. Impact of pulse parameters on the seismic response of long-period bridges. Structure and Infrastructure Engineering 2020;16:1461-1480. http://doi.org/10.1080/15732479.2020.1712734

[21] Yang T, Wei Y, Zhong J. Potential bias of conventional structural seismic fragility for bridge structures under pulse-like ground motions: Bias evaluation and strategy improvement. Soil Dynamics and Earthquake Engineering 2023;166:107787. https://doi.org/10.1016/j.soildyn.2023.107787

[22] Yang T, Yuan X, Zhong J, Yuan W. Near-fault pulse seismic ductility spectra for bridge columns based on machine learning. Soil Dynamics and Earthquake Engineering 2023;164:107582. https://doi.org/10.1016/j.soildyn.2022.107582

[23] Shen Y, Gao B, Yang X, Tao S. Seismic damage mechanism and dynamic deformation characteristic analysis of mountain tunnel after Wenchuan earthquake. Engineering Geology 2014;180:85-98. http://doi.org/10.1016/j.enggeo.2014.07.017

[24] Wang WL, Wang TT, Su JJ, Lin CH, Seng CR, Huang TH. Assessment of damage in mountain tunnels due to the Taiwan Chi-Chi earthquake. Tunnelling and Underground Space Technology 2001;16:133-150.

http://doi.org/10.1016/S0886-7798(01)00047-5

[25] Kontoe S, Zdravkovic L, Potts DM, Menkiti CO. Case study on seismic tunnel response. Canadian Geotechnical Journal 2008;45:1743-1764. http://doi.org/10.1139/T08-087

[26] Yu H, Chen J, Bobet A, Yuan Y. Damage observation and assessment of the Longxi tunnel during the Wenchuan earthquake. Tunnelling and Underground Space Technology 2016;54:102-116. http://doi.org/10.1016/j.tust.2016.02.008

[27] Qiu D, Chen J, Xu Q. 3-D numerical analysis on seismic responses of the underground large scale frame structure under near-fault ground motions. Tunnelling and Underground Space Technology 2019;91:103020. http://doi.org/10.1016/j.tust.2019.103020

[28] Cui Z, Sheng Q, Leng X. Effects of a controlling geological discontinuity on the seismic stability of an underground cavern subjected to near-fault ground motions. Bulletin of Engineering Geology and the Environment 2018;77:265-282. http://doi.org/10.1007/s10064-016-0936-9

[29] Chen Z, Wei J. Correlation between ground motion parameters and lining damage indices for mountain tunnels. Natural Hazards 2013;65:1683-1702. http://doi.org/10.1007/s11069-012-0437-5

[30] Sun B, Zhang S, Deng M, Wang C. Inelastic dynamic response and fragility analysis of arched hydraulic tunnels under as-recorded far-fault and near-fault ground motions. Soil Dynamics and Earthquake Engineering 2020;132:106070. http://doi.org/10.1016/j.soildyn.2020.106070

[31] Chen Z, Chen W, Li Y, Yuan Y. Shaking table test of a multi-story subway station under pulse-like ground motions. Soil Dynamics and Earthquake Engineering 2016;82:111-122. http://doi.org/10.1016/j.soildyn.2015.12.002

[32] Yang Y, Yu H, Yuan Y, Sun J. 1 g Shaking table test of segmental tunnel in sand under near-fault motions. Tunnelling and Underground Space Technology 2021;115:104080. http://doi.org/10.1016/j.tust.2021.104080

[33] de Barros FCP, Luco JE. Diffraction of obliquely incident waves by a cylindrical cavity embedded in a layered viscoelastic half-space. Soil Dynamics and Earthquake Engineering 1993;12:159-171. http://doi.org/https://doi.org/10.1016/0267-7261(93)90043-Q

[34] Huang J, Du X, Jin L, Zhao M. Impact of incident angles of P waves on the dynamic responses of long lined tunnels. Earthquake Engineering & Structural Dynamics 2016;45:2435-2454. http://doi.org/10.1002/eqe.2772

[35] Li P, Song E. Three-dimensional numerical analysis for the longitudinal seismic response of tunnels under an asynchronous wave input. Computers and Geotechnics 2015;63:229-243. http://doi.org/10.1016/j.compgeo.2014.10.003

[36] Stamos AA, Beskos DE. 3-D seismic response analysis of long lined tunnels in half-space. Soil Dynamics and Earthquake Engineering 1996;15:111-118. http://doi.org/https://doi.org/10.1016/0267-7261(95)00025-9

[37] Hashash YMA, Hook JJ, Schmidt B, Yao JI. Seismic design and analysis of underground structures. Tunnelling and Underground Space Technology 2001;16:247-293. http://doi.org/10.1016/S0886-7798(01)00051-7

[38] Pitilakis K, Tsinidis G. Performance and seismic design of underground structures, In: Maugeri M, Soccodato C (eds), Earthquake geotechnical engineering design. Springer; 2014, pp. 279-340. http://doi.org/10.1007/978-3-319-03182-8_11

[39] Han B, Zdravković L, Kontoe S. Analytical and numerical investigation of site response due to vertical ground motion. Géotechnique 2018;68:467-480. http://doi.org/10.1680/jgeot.15.P.191

[40] Scanlan RH, Sachs K. Earthquake time histories and response spectra. Journal of the Engineering Mechanics Division 1974;100:635-655. https://doi.org/10.1061/JMCEA3.0001911

[41] He Q, Li X, Yang Y. Displacement response analysis of base-isolated buildings subjected to near-fault ground motions with velocity pulse. Journal of Basic Science and Engineering 2014;22(1):1-13. http://doi.org/10.3969/j.issn.1005-0930.2014.01.001

[42] Biot MA. Theory of propagation of elastic waves in a fluid-saturated porous solid. I. Low-frequency range. Journal of the Acoustical Society of America 1956;28:168-178. http://doi.org/10.1121/1.1908239

[43] Biot MA. Mechanics of deformation and acoustic propagation in porous media. Journal of Applied Physics

1962;18:1482-1498. http://doi.org/10.1063/1.1728759

[44] Biot MA, Willis DG. The elastic coefficients of the theory of consolidation. Journal of Applied Mechanics 1957;24:594–601. https://doi.org/10.1115/1.4011606

[45] Lin C, Lee VW, Trifunac MD. The reflection of plane waves in a poroelastic half-space saturated with inviscid fluid. Soil Dynamics and Earthquake Engineering 2005;25:205-223. https://doi.org/10.1016/j.soildyn.2004.10.009

[46] Cheng AHD. Poroelasticity. Switzerland: Springer International Publishing; 2016. https://doi.org/10.1007/978-3-319-25202-5

[47] Zhu J, Liang J, Ba Z. A 2.5D equivalent linear model for longitudinal seismic analysis of tunnels in water-saturated poroelastic half-space. Computers and Geotechnics 2019;109:166-188. http://doi.org/10.1016/j.compgeo.2018.12.021

[48] François S, Schevenels M, Galvín P, Lombaert G, Degrande G. A 2.5D coupled FE-BE methodology for the dynamic interaction between longitudinally invariant structures and a layered halfspace. Computer Methods in Applied Mechanics and Engineering 2010;199:1536-1548. http://doi.org/10.1016/j.cma.2010.01.001

[49] Liang J, Ba Z. Exact dynamic stiffness matrices of 3-D layered site and its Green's functions. Journal of Earthquake Engineering and Engineering Vibration 2007;27(5):7-17. http://doi.org/10.3969/j.issn.1000-1301.2007.05.002

[50] Liang J, Wu M, Ba Z. IBEM simulation of three-component scattering of elastic waves in fluid-saturated half-space with 2D topography. Chinese Journal of Geophysics 2021;64(8):2766-2779. http://doi.org/10.6038/cjg2021O0248

[51] Wolf JP. Dynamic Soil-Structure Interaction. Englewood Cliffs: Prentice-Hall; 1985.

[52] Bentley Systems. CONNECT Edition V22.01 PLAXIS 2D-Reference Manual, 2022.

[53] Tsaparli V, Kontoe S, Taborda DMG, Potts DM. The importance of accurate time-integration in the numerical modelling of P-wave propagation. Computers and Geotechnics 2017;86:203-208. http://doi.org/10.1016/j.compgeo.2017.01.017

[54] Wang JN. Seismic design of tunnels: A simple state-of-the-art design approach. New York: Parsons Brinckerhoff Inc.; 1993.

[55] Kontoe S, Zdravkovic L, Potts DM, Menkiti CO. On the relative merits of simple and advanced constitutive models in dynamic analysis of tunnels. Géotechnique 2011; 61(10):815-829. https://doi.org/10.1680/geot.9.P.141